Abrupt excursions in water vapor isotopic variability ~~during cold fronts~~ at the Pointe Benedicte observatory ~~in~~ on Amsterdam Island

Amaëlle Landais[1,*], Cécile Agosta[1,*], Françoise Vimeux[1,2], Olivier Magand[3], Cyrielle Solis[1], Alexandre Cauquoin[4], Niels Dutrievoz[1], Camille Risi[5], Christophe Leroy-Dos Santos[1], Elise Fourré[1], Olivier Cattani[1], Olivier Jossoud[1], Bénédicte Minster[1], Frédéric Prié[1], Mathieu Casado[1], Aurélien Dommergue[6], Yann Bertrand[6], Martin Werner[7]

[1] Laboratoire des Sciences du Climat et de l'Environnement, LSCE/IPSL, CEA-CNRS-UVSQ, Université Paris-Saclay, 91191 Gif-sur-Yvette, France

[2] HydroSciences Montpellier (HSM), UMR 5569 (UM, CNRS, IRD), 34095 Montpellier, France

[3] Observatoire des Sciences de l'Univers à La Réunion (OSU-R), UAR 3365, CNRS, Université de La Réunion, Météo France, IRD, 97744 Saint-Denis, La Réunion, France

[4] Institute of Industrial Science (IIS), The University of Tokyo, Kashiwa, Japan.

[5] Laboratoire de Météorologie Dynamique, Institut Pierre - Simon Laplace, Sorbonne Université / CNRS / École Polytechnique – IPP, Paris, France

[6] Univ. Grenoble Alpes, CNRS, INRAE, IRD, Grenoble INP[ᵀ], IGE, 38000 Grenoble, France ([ᵀ]Institute of Engineering and Management Univ. Grenoble Alpes)

[7] Alfred Wegener Institute, Helmholtz Centre for Marine and Polar Research, D-27570 Bremerhaven, Germany

* corresponding authors who contributed equally to the study: amaelle.landais@lsce.ipsl.fr and cecile.agosta@lsce.ipsl.fr

Abstract

In order to complement the picture of the atmospheric water cycle in the Southern Ocean, we have continuously monitored water vapor isotopes since January 2020 o~~i~~n Amsterdam Island ~~(37.7983 °S, 77.5378 °E)~~ in the Indian Ocean. We present here the first 2-year-long water vapor isotopic record ~~monitored~~ on this site. We show that the water vapor isotopic composition largely follows the water vapor mixing ratio, as expected in marine boundary layers. However, we ~~evidence~~ detect 11 ~~cold front~~ periods of a few days where there is a strong loss of correlation between water vapor $\delta^{18}O$ and water vapor mixing ratio~~. These periods are associated with~~ as well as abrupt negative excursions of water vapor $\delta^{18}O$. These excursions~~,~~ often occur~~ring~~ toward the end of precipitation events. Six of these events show a decrease in gaseous elemental mercury suggesting subsidence of air from higher altitude.

Our study aims at further exploring the mechanism driving these negative excursions in water vapor $\delta^{18}O$. We used two different models to provide a data-model comparison over this 2-year period. ~~Accurately representing the water isotopic signal during these cold fronts is a real challenge for the atmospheric components of Earth System models equipped with water isotopes. W~~While the European Centre Hamburg model (ECHAM6-wiso) at 0.9° ~~model~~ was able to reproduce most of the sharp negative water vapor $\delta^{18}O$ excursions hence validating the physics process and isotopic implementation in this model, the Laboratoire de Météorologie Dynamique Zoom model (LMDZ-iso)~~ model~~ at 2° (3°) resolution was only able to reproduce 7 (1) of the negative excursions highlighting the possible influence of the model resolution for the study of such abrupt isotopic events.~~ Based on a our detailed model-data comparison, we conclude that the most plausible explanations for such isotopic excursions are rain-vapor interactions associated with subsidence at the rear of a precipitation event.

Mis en forme: Couleur de police : Automatique

Mis en forme: Couleur de police : Automatique

1. Introduction

The main sources of uncertainty in the atmospheric components of Earth System Models for future climate projections are associated with complex atmospheric processes, particularly those related to water vapor and clouds (Arias et al., 2021; Sherwood et al., 2014~~; Arias et al., 2021~~). Decreasing these uncertainties is of vital interest as the hydrological cycle is a fundamental element of the climate system because it allows, via the transport of water vapor, to ensure the Earth's thermal balance.

Stable water isotopes are a useful tool to study the influence of dynamical processes on the water budget at various spatial and temporal scales. They provide a framework for analyzing moist processes over a range of time scales from large-scale moisture transport to cloud formation, precipitation, and small-scale turbulent mixing (Bailey et al., 2023; Dahinden et al., 2021; Galewsky et al., 2016; Thurnherr et al., 2020~~; Bailey et al., 2023; Dahinden et al., 2021~~). The relative abundance of heavy and light isotopes in different water reservoirs is altered during phase change processes due to isotopic fractionation (caused by a difference in saturation vapor pressure and molecular diffusivity in the air and the ice). Each time a phase change occurs, the relative abundance of water vapor isotopes is altered. We express the abundance of the heavy isotopes D and ^{18}O with respect to the amount of light isotopes H and ^{16}O, respectively, ~~and H~~ in the water molecules through the notation δ:

$$\delta^{18}O = \left(\frac{\left({}^{18}\square O / {}_{16}\square O \right)_{Sample}}{\left({}^{18}\square O / {}_{16}\square O \right)_{VSMOW}} - 1 \right) \times 1000 \qquad \text{(Eq. 1)}$$

$$\delta D = \left(\frac{\left(D / H \right)_{Sample}}{\left(D / H \right)_{VSMOW}} - 1 \right) \times 1000 \qquad \text{(Eq. 2)}$$

where ($^{18}O/^{16}O$) and (D/H) represent the isotopic ratios of oxygen and hydrogen atoms in water and VSMOW (Vienna Standard Mean Ocean Water) is an international reference standard for water isotopes.

There are two types of isotopic fractionation: equilibrium fractionation, which is caused by the difference in saturation vapor pressure of different isotopes, and non-equilibrium fractionation, which occurs due to molecular diffusion (e.g. during ocean evaporation in undersaturated atmosphere or snowflakes condensation in oversaturated atmosphere). In the water vapor above the ocean, the proportion of non-equilibrium fractionation, and hence diffusive processes can

Mis en forme: Exposant

Mis en forme: Exposant

be estimated by the deuterium excess, a second order isotopic variable denoted d-excess, defined as (Dansgaard, 1964):

$$d\text{-excess} = \delta D - 8 \times \delta^{18}O \qquad \text{(Eq.3)}$$

Over the recent years and thanks to the development of optical spectroscopy enabling continuous measurements of water isotopes ratios in water vapor, an increasing number of studies have focused on the use of water vapor stable isotopes ~~in water vapor~~ to document the dynamics of the water cycle over synoptic weather events, such as cyclones, cold fronts, atmospheric rivers (~~Tremoy et al., 2014;~~ Aemisegger et al., 2015; Ansari et al., 2020; Bhattacharya et al., 2022; ~~Munksgaard et al., 2015;~~ Dütsch et al., 2016; Graf et al., 2019; Lee et al., 2019; ~~Ansari et al., 2020; Bhattacharya et al., 2022~~ Munksgaard et al., 2015; Tremoy et al., 2014) or water cycle processes ~~such as water cycle processes~~ such as evaporation over the ocean or deep convection (Benetti et al., 2015; Bonne et al., 2019~~; Benetti et al., 2015~~). ~~For this objective, s~~Several instruments have been installed either in observatory stations (e.g. Aemisegger et al., 2012; Guilpart et al., 2017; Leroy-Dos Santos et al., 2020; Steen-Larsen et al., 2013; Tremoy et al., 2012~~; Guilpart et al., 2017; Steen-Larsen et al., 2013; Leroy-Dos Santos et al., 2020; Aemisegger et al., 2012~~), ~~or~~ on boat (e.g. Benetti et al., 2014; Thurnherr et al., 2019~~; Benetti et al., 2014~~) or on aircraft (Henze et al., 2022). In the aforementioned studies, the interpretation of the isotopic records is often performed using a hierarchy of isotopic models, from conceptual models (Rayleigh type) to general circulation models or regional weather prediction models equipped with water isotopes (Ciais and Jouzel, 1994; Markle and Steig, 2022; Risi et al., 2010; Werner et al., 2011~~; Ciais and Jouzel, 1994; Markle and Steig, 2022~~). Such data comparisons enable~~s~~ one to test the performances of the models either in the simulation of the dynamic of the atmospheric water cycle or in the implementation of the water isotopes.

Our study is part of these dynamics analyses and aims at improving the documentation of climate and atmospheric water cycle in the Southern Indian Ocean, a region which has been poorly documented until now. ~~This region is poorly documented with present-day observations despite its primary importance in governing CO_2 sinks. Moreover, we lack precise descriptions of atmospheric processes associated with cloud microphysics and surface-atmosphere exchange in polar regions, and the evolution of westerly wind locations and strength (Fogt and Marshall, 2020).~~

Over the previous years, we have installed ~~3~~ three water vapor analyzers on La Reunion Island at the Maïdo observatory, ~~(~~21.079°S, 55.383°E, 2160m~~)~~ (Guilpart et al., 2017) and in Antarctica (Dumont d'Urville, 66,663°S, 140°E, 202m ~~–~~and Concordia, 75.1°S, 123.333°E, 3233m; ~~(Leroy-Dos Santos et al., 2021;~~ Bréant et al., 2019; Casado et al., 2016; Leroy-Dos Santos et al., 2021). These instruments have been used for the following purposes. They document the diurnal variability of the isotopic signal with the influence of the subtropical westerly jet on the water isotopic signal ~~at~~ in night as well as the cyclonic activity ~~in~~on La Réunion Island. In Antarctica, the records~~instruments~~ have shown a strong influence of katabatic winds on the isotopic composition of ~~the~~ water vapor (Bréant et al., 2019). In order to complete the picture of the atmospheric water cycle over the Indian basin of the Southern Ocean already measured~~documented~~ by these three analyzers, we installed a new water vapor isotopic analyzer in the mid-latitude of the south Indian Ocean on Amsterdam Island (Figure 1) in November 2019. Amsterdam Island is one of the very rare atmospheric observatories in the southern hemisphere. Moreover, the south Indian Ocean is a significant moisture source for Antarctic precipitation, notably in the region encompassing Dumont d'Urville and Concordia stations (Jullien et al., 2020; Wang et al., 2020).

The objective of this study is to provide the first analyses of isotopic records (vapor and precipitation) o~~i~~n Amsterdam Island, with a comparison of meteorological data and environmental data collected in parallel on the Amsterdam Island Observatory (e.g. atmospheric mercury) to help with the interpretation of isotopic records. This study includes analyses of meteorological maps, back trajectories as well as outputs from general circulation models equipped with water isotopes. After a description of the different records over the years 2020 and 2021, model simulations and back trajectories~~y methodology~~, we focus on some low-pressure events ~~(cold fronts)~~ associated with a strong negative excursion of ~~the~~ $\delta^{18}O_v$ ~~of water vapor~~ over a few days and a decoupling between $\delta^{18}O_v$ and humidity. These events~~, expressed strongly in the water vapor isotopic record,~~ are then used for evaluation of to evaluate atmospheric component of Earth system models ~~general circulation models~~ equipped with water isotopes.

2. Methods

2.1 Site

Labelled as a global site for the ~~GAW WMO (~~Global Atmosphere Watch World Meteorological Organization~~) global site~~, Amsterdam Island (37.7983~~°~~ S, 77.5378~~°~~ E) is a remote and very

small island of 55 km^2 with a population of about 30 residents, located in the southern Indian Ocean at 3300 km and 4200 km downwind from the nearest lands, Madagascar, and South Africa, respectively (Sprovieri et al., 2016). Climate is temperate, generally mild with frequent presence of clouds (average total sunshine hours is 1581 hours per year over the period 1981 – 2010 from MeteoFrance data). Seasonal boundaries ~~a~~were defined as follows: winter from July to September and summer from December to February, in line with previous studies (Sciare et al., 2009). Average temperature is lower in winter compared to summer (10.5°C vs 15°C) while relative humidity and wind speed remain high (~~respectively~~ 50-85% and 5 to 15 m s^{-1} respectively) most of the year without a clear seasonal cycle.

Numerous atmospheric compounds and meteorological parameters are and were continuously monitored at the site ~~from~~ since 1960 (Angot et al., 2014; El Yazidi et al., 2018; Gaudry et al., 1983; Gros et al., 1999, 1998; Polian et al., 1986; ~~Gros et al., 1999, 1998;~~ Sciare et al., 2000, 2009; ~~Angot et al., 2014;~~ Slemr et al., 2015; ~~El Yazidi et al., 2018;~~ Slemr et al., 2020). In particular, the Amsterdam (AMS) site hosts several dedicated atmospheric observation instruments notably at the Pointe Bénédicte atmospheric observatory (70 m above sea level) where greenhouse gases ~~(GES)~~ concentrations and mercury (Hg) ~~species~~ are monitored. ~~(service ICOS France Atmosphère, ICOS AMS 416 IPEV program, GMOStral 1028 IPEV program). Both GES and Hg species measurements respond to international monitoring networks (ICOS https://www.icos-cp.eu/, GEO GOS4M http://www.gos4m.org/ for GES and Hg species respectively). CO_2, CO, CH_4, and~~ Hg species have been continuously measured since ~~1980, 2014, and~~ 2012 ~~respectively~~.

Figure 1 : Location (left) and picture (right) of ~~the~~ Amsterdam Island. CRO: Crozet Island; RUN: La Réunion I~~i~~sland; KER: Kerguelen Island; AMS: Amsterdam Island. Picture credit: left – Magand adapted from (Angot et al., 2016); right – photo taken by O. Magand.

2.2 Long term measurements

2.2.1 Meteorological measurements

One~~Two~~ meteorological station~~s~~ is ~~are~~ installed at the top of an observation mast (25 m above ground level, hence 95 m above sea level~~, agl~~) at the Pointe Bénédicte observatory ~~(data used during this study),~~ since 1980 (data used during this study). ~~Installed and managed by ICOS-AMS-416-IPEV program, w~~Wind speed and direction, atmospheric pressure, air~~surface~~ temperature and relative humidity data are currently ~~measured by a WXT520 Vaisala weather system. Data~~ obtained at a minute resolution. ~~(minute acquisition frequency) are cleaned and processed by the IGE in the framework of the GMOStral-1028 IPEV program.~~ Another meteorological station is based on the island and is operated by Météo France at Martin-de-~~Viviegs~~ Viviès life base around 27 m above sea level, about two kilometers east from the Pointe Bénédicte observatory collecting ~~.~~ ~~This second weather station collects~~ air temperature, humidity, precipitation, wind speed and direction, pressure and solar radiation ~~via a mercury SYNOP automatic weather station from STERELA meteo company. Only daily precipitation data provided by Meteo France are used in the current study.~~

2.2.2 Gaseous elemental mercury (GEM)

Atmospheric GEM (Gaseous Elemental Mercury) measurements have been ~~are~~ conducted since 2012 in the framework of IPEV GMOStral-1028 observatory program at the Pointe Benedicte atmospheric research facility ~~. Data are freely available on the national GMOS-FR data platform AERIS (~~(Magand and Dommergue, 2022)~~) (https://gmos.aeris-data.fr, last access: 07/12/2022)~~.

GEM is continuously measured (15~~-~~minute data frequency acquisition) using a Tekran 2537 A/B instrument model~~s~~ ~~(Tekran Inc., Toronto, Canada)~~ (Angot et al., 2014; Li et al., 2023; Slemr et al., 2015, 2020; Sprovieri et al., 2016~~; Li et al., 2023~~). The measurement~~operation device~~ is based on mercury enrichment on a gold cartridge, followed by ~~a~~ thermal desorption

and ~~a~~ detection by cold vapor atomic fluorescence spectroscopy ~~(CVAFS) at 253.7 nm~~ (Bloom and Fitzgerald, 1988; Fitzgerald and Gill, 1979~~; Bloom and Fitzgerald, 1988~~). ~~Switching between two cartridges allows for alternating sampling and desorption and thus results in a quasi-continuous temporal coverage of the mercury measurement since the last decade.~~ Concentrations are expressed in nanograms per cubic meters at ~~STP~~ standard temperature and pressure conditions (2~~1~~73.15 K and 1013.25 hPa) with an instrumental detection limit below 0.1 ng m^{-3} and a GEM average uncertainty value around 10% (Slemr et al., 2015). The instrument is automatically calibrated following a strict procedure adapted from that of Dumarey et al. (1985). Ambient air is sampled at 1.2 L min^{-1} through a heated (50°C) and UV protected PTFE sampling line, with an inlet installed outside, 6 m above ground level (76 m above sea level). The air is filtered through two 0.45 µm pore size polyether sulphone ~~(PES)~~ and one PTFE (polytetrafluoroethylene) 47 mm diameter filters before entering in ~~the~~ Tekran to prevent the introduction of any particulate material into the detection system as well as to capture any ~~GOM (Gaseous~~ gaseous ~~Oxidised~~ oxidized ~~Mercury~~mercury~~)~~ or particulate bound mercury ~~(PBM)~~ species ensuring that only GEM is sampled. To ensure the comparability of ~~Hg~~mercury measurements around the world, the instrument is operated according to the Global Mercury Observation System ~~(GMOS) and CAMNET, AMNET~~ standard operating procedures (Sprovieri et al., 2016; Steffen et al., 2012~~; Sprovieri et al., 2016~~). ~~The detailed quality assurance and quality control required by GMOS to produce qualified dataset are described in detail in the GMOS-FR data products section in GMOS-FR website data portal (https://gmos.aeris-data.fr last access: 07/12/2022)~~.

In this study, and even if long-range transport and a variable tropopause height may modulate the signal, atmospheric GEM is used as potential tracer of stratosphere-to-troposphere intrusion and/or subsidence of upper troposphere (above 5-6 km) that may impact the atmospheric records at the Pointe Benedicte Observatory where marine boundary layer is collected most of the time ~~In this study, atmospheric GEM is used as potential tracer of intrusion and/or subsidence of high altitude air masses (lower/ upper troposphere, or even above) that may possibly impact the atmospheric records in Pointe Benedicte Observatory which collects marine boundary layer most of the time~~ (Angot et al., 2014 ; Slmer et al., 2015, 2020; Sprovieri et al., 2016 ~~; Slmer et al., 2015, 2020~~). Mercury in the atmosphere consists of three forms: gaseous elemental mercury (GEM as defined above), gaseous oxidized mercury and particulate-bound mercury. ~~As mentioned above, mercury in the atmosphere is detected in three defined forms: GEM, GOM (HgO, $HgCl_2$, $HgBr_2$, $Hg[OH]_2$) and PBM.~~ GEM, the dominant form of atmospheric mercury ~~species~~, is ubiquitous in the atmospheric reservoir and originates from a

Mis en forme: Couleur de police : Automatique

multitude of anthropogenic and natural sources (Edwards et al., 2021; Gaffney et al., 2014 ; Gustin et al., 2020 ; Gworek et al., 2020 ; ~~Gustin et al., 2020 ; Edwards et al., 2021~~). Near the surface (marine or terrestrial boundary layer) and out of polar regions, ~~GOM~~ gaseous oxidized mercury and particulate-bound mercury~~PBM~~ represent only a few percent of the total atmospheric mercury (Gustin and Jaffe, 2010 ; Gustin et al., 2015; Swartzendruber et al., 2006~~;~~ ~~Gustin and Jaffe, 2010 ; Gustin et al., 2015~~). ~~Even if c~~Chemical cycling and spatiotemporal distribution of mercury in the air~~,~~ is still poorly understood whatever atmospheric layer considered (surface, mixed or free troposphere, stratosphere), ~~is still poorly understood~~ and complete GEM oxidation schemes remain ~~still~~ unclear (Shah et al., 2021 and associated references). Still,~~,~~ several studies provided evidence that vertical distribution of atmospheric mercury measurements from boundary layer to lower/upper troposphere and stratosphere shows a decreasing trend in GEM concentration with increasing altitude, in parallel with an increase in the concentration of divalent mercury ~~(GOM + PBM)~~ resulting from GEM oxidation mechanisms (Brooks et al., 2014 ; Fain et al., 2009 ; Fu et al., 2016 ; Koenig et al., 2023; Lyman and Jaffe, 2012; Murphy et al., 2006 ; Swartzendruber et al., 2006, 2008 ; Sheu et al., 2010 ; Talbot et al., 2007~~; Fain et al., 2009 ; Sheu et al., 2010 ; Lyman and Jaffe, 2012 ; Brooks et al., 2014 ; Fu et al., 2016 ; Koenig et al., 2023~~). The identification of such observational processes (lower GEM concentrations in high-altitude air masses versus marine boundary layer ones) is used here to help characterizing possible high altitude air masses ~~excursion~~ intrusions at~~in~~ low altitude Pointe Benedicte Observatory.

2.3 Water vapor isotopic measurements

The ~~isotopic composition of~~ near-surface water vapor $\delta^{18}O$ and δD ~~-~~(hereafter $\delta^{18}O_v$ and δD_v expressed in ‰ versus SMOW and enabling to calculate water vapor d-excess$_v$ as d-excess$_v$ = $\delta D_v - 8\times\delta^{18}O_v$) and the water vapor mixing ratio (q_v in ppmv) have been measured continuously since November 2019. The measurements have been done with a Picarro Inc. instrument (L2130-~~I~~i model) based on wavelength-scanned cavity ring down spectroscopy. The instrument has been installed in a temperature-controlled room at the ~~observatory on the~~ Amsterdam Island observatory and the sampling of water vapor is done outside at ~ 6 m above ground level (or 76 m above sea level) through a 5 m long inlet tube made of PFA (perfluoroalkoxy alkanes) and heated at 40°C.

Mis en forme: Non Exposant/ Indice
Mis en forme: Indice
Mis en forme: Indice
Mis en forme: Police :Symbol
Mis en forme: Indice
Mis en forme: Police :Symbol
Mis en forme: Exposant
Mis en forme: Indice

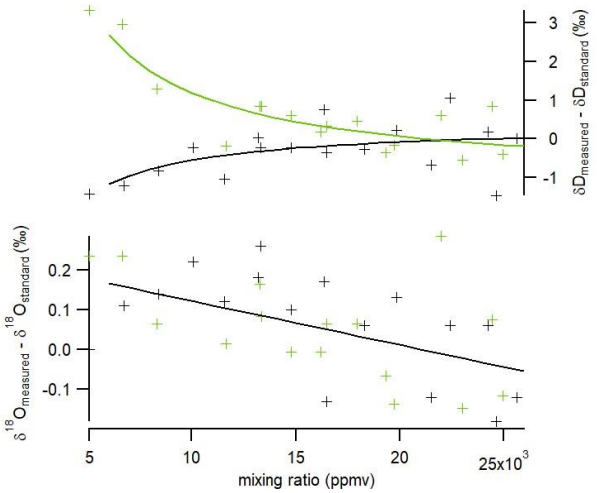

Figure 2: ~~Dependency~~ Influence of the water vapor mixing ratio on~~of~~ measured ~~-~~δD (top) and $\delta^{18}O$ (bottom) (anomaly from the true value of the standard)~~ on the mixing ratio~~. The results are shown for two different standards (GREEN_AMS in green and EPB_AMS in black). The crosses indicate the data obtained with the set-up and the solid lines are the best regression curves (same curve~~s~~ for $\delta^{18}O$ for both standards).

The calibration of water vapour mixing ratio was performed in the laboratory before sending the instrument. In the field, we found an excellent agreement between mixing ratio measured by the Picarro instrument and mixing ratio measured by the weather station (the difference between the two records always stays below 2% and there is no systematic shift between the two records).

The calibration of the water isotopic data is performed in ~~different~~ several steps following previous studies (Leroy-Dos Santos et al., 2020; Tremoy et al., 2011~~; Leroy-Dos Santos et al., 2020~~) and using a standard delivery module by Picarro. First, we quantified the influence of the water vapor mixing ratio on the water isotope ratios. This effect is large at very low humidity (Leroy-Dos Santos et al., 2021). It can also depend on the isotopic composition of the standard water (Weng et al., 2020). Here, we introduced two different water standards, EPB-AMS and GREEN-AMS, with respective values of (-5.66 ‰, -47.31 ‰) and (-32.65 ‰, -263.76 ‰) for the couple ($\delta^{18}O$, δD) which encompass the isotopic values observed on site ~~observations~~. While we would expect a constant null value for ($\delta^{18}O_{measured}$ - $\delta^{18}O_{standard}$) in Figure 2 because we always inject the same water standards, the measured $\delta^{18}O$ values of

Mis en forme: Couleur de police : Automatique

both EPB-AMS and GREEN-AMS standards in fact decrease with increasing humidity with the same amplitude. The ($\delta D_{measured}$-$\delta D_{standard}$) displayed in Figure 2 also shows variations but in contrast to the relative evolution of $\delta^{18}O$ with respect to water vapor mixing ratio, the δD measurements of EPB-AMS and GREEN-AMS standards exhibit different behavior: δD of EPB-AMS increases by 1.5‰ and δD of GREEN-AMS decreases by 2.5 ‰ over the same 6,000-24,000 ppmv range for water vapor mixing ratio q_v. ~~The $\delta^{18}O$ measurements of both EPB-AMS and GREEN-AMS standards decrease with increasing humidity with the same amplitude. In contrast, the δD measurements of both EPB-AMS and GREEN-AMS standards exhibit different behavior: δD of EPB-AMS increases by 1.5‰ and δD of GREEN-AMS decreases by 2.5 ‰ over the same 6,000-24,000 ppmv range for mixing ratio q_v.~~

As a consequence, the raw $\delta^{18}O_v$ measurements are corrected with the following regression:

$$\delta^{18}O_{v,corr} = \delta^{18}O_{v,measured} + 1.1.10^{-5} \times q + 0.232 \qquad (Eeq\ 4)$$

Mis en forme: Police :12 pt

For the correction of the raw δD_v, we use two different regression splines for EPB-AMS and GREEN-AMS (cf Figure 2):

$$\delta D_{EPB-AMS,corr} = \delta D_{EPB-AMS,measured} + \frac{9300}{q} - 0.383 \qquad (Eeq\ 5)$$

$$\delta D_{GREEN-AMS,corr} = \delta D_{GREEN-AMS,measured} - \frac{22400}{q} + 1.05 \qquad (Eeq\ 6)$$

The raw δD_v are thus weighted-corrected according to their distance ~~of the measured δD value from~~to the EPB_AMS and the GREEN_AMS splines as follows:

$$\delta D_{v,corr} = \delta D_{GREEN-AMS,corr} + \frac{\delta D_{v,measured} - \delta D_{GREEN-AMS,measured}}{\delta D_{EPB-AMS,measured} - \delta D_{GREEN-AMS,measured}} \times (\delta D_{EPB-AMS,corr} - \delta D_{GREEN-AMS,corr})$$

(eq 7)

This first calibration step (correction from the influence of mixing ratio on the isotopic composition) has been performed every year over the whole range of mixing ratio values and provided very similar results from one year to the other.

The second calibration step consists in the injection of the same two isotopic standards every 47 h at a water vapor mixing ratio of 13,000 ppmv to correct for any long-term drift. The correction associated with this drift is less than 0.4 ‰ for $\delta^{18}O$ and 2.5 ‰ for δD over the two years of measurements.

Precipitation were also sampled on a weekly basis in a rain gauge filled with paraffin oil which permits to have measurements of water isotopic composition in the precipitation on a weekly basis. The water samples are then sent for analyses ~~at~~ to LSCE (Laboratoire des Sciences du Climat et de l'Environnement) and measured ~~on~~with an isotopic analyzer L2130-~~i~~I by Picarro. The uncertainty associated with this series of measurements is of ±0.15 ‰ for $\delta^{18}O$ and ±0.7 ‰ for δD leading to ~~a quadratic error~~an uncertainty of ±1.4 ‰ for d-excess.

2.4 Back trajectories: FLEXPART

The origin and trajectory of air masses were ~~assessed~~ calculated by FLEXPART, which is a Lagrangian particle dispersion model (Pisso et al., 2019). All the meteorological data used to simulate the back trajectories are taken from the ERA5 atmospheric reanalysis (Hersbach et al., 2020) with a 6-hourly resolution. The ERA5 reanalysis is carried out by the European Center for Medium-Range Weather Forecasts (ECMWF), using ECMWF's Earth System model IFS (Integrated Forecasting System), cycle 41r2. For a few selected events, we used FLEXPART to calculate~~d~~ back trajectories over ~~10~~5 days with 1000 launches of neutral particles (sensitivity test) of inert air tracers released randomly (volume of 0.1°×0.1°×100 m) every 3 hours at 100 m ~~altitude~~ above sea level (Leroy-Dos Santos et al., 2020)~~,~~ centered around the coordinates of Amsterdam Island. The results of the FLEXPART back trajectories are then displayed ~~in~~ as particle density probability as well as through the location of their humidity weighted averages.

2.5 General atmospheric circulation model equipped with water stable isotopes

2.5.1 LMDZ-iso model (Laboratoire de Météorologie Dynamique Zoom model equipped with water isotopes)

LMDZ-iso (Risi et al., 2010) is the isotopic version of the atmospheric general circulation model LMDZ6 (Hourdin et al., 2020). We have used LMDZ-iso version 20230111.trunk with

Mis en forme: Gauche

Mis en forme: Couleur de police : Automatique

Mis en forme: Police :(Par défaut) Times New Roman

the physical package NPv6.1, identical ~~as~~ to the atmospheric setup of IPSL-CM6A (Boucher et al., 2020) used for phase 6 of the Coupled Model Intercomparison Project (CMIP6, ~~(~~Eyring et al., 2016)~~)~~. We performed two simulations, one at very low horizontal resolution (VLR, 3.75° in longitude and 1.9° in latitude, 96×95 grid cells) and the second at low horizontal resolution (LR, 2.0° in longitude and 1.67° in latitude, 144×142 grid cells). Both simulations have 79 vertical levels and the first atmospheric level is located around 10 m above ground level. The LMDZ-iso 3D-fields of temperature and wind are nudged toward the 6-hourly ERA5 reanalysis data with a relaxation time of 3 hours. Surface ocean surface boundary conditions are taken from the monthly mean SST and sea-ice fields from the CMIP6 AMIP Sea Surface Temperature and Sea Ice dataset version 1.1.8 (Durack et al., 2022; Taylor et al., 2000). LMDZ-iso outputs are used at a 3-hourly resolution. ~~The~~ Amsterdam Island (58 km^2) is too small to be represented in the LMDZ-iso model.

2.5.2 ECHAM6-wiso model (European Centre Hamburg model equipped with water isotopes)

ECHAM6-wiso (Cauquoin et al., 2019; Cauquoin and Werner, 2021) is the isotopic version of the atmospheric general circulation model ECHAM6 (Stevens et al., 2013). The implementation of the water isotopes in ECHAM6 has been described in detail by Cauquoin et al. (2019), and has been updated in several aspects by Cauquoin and Werner (2021) to make the model results more consistent with the last findings based on water isotope observations (isotopic composition of snow on sea ice considered, supersaturation equation slightly updated, and kinetic fractionation factors for oceanic evaporation assumed as independent of wind speed). We have used ECHAM6-wiso model outputs from a simulation ~~at~~ with a T127L95 ~~high~~ spatial resolution (0.9° horizontal resolution and 95 vertical levels)~~, nudged to ERA5 reanalysis (Hersbach et al., 2020).~~ ECHAM6-wiso is thus run with a finer resolution than both LMDZ-iso simulations. The ECHAM6-wiso 3D-fields of temperature, vorticity and divergence as well as the surface pressure field were nudged toward the ERA5 reanalysis data (Hersbach et al., 2020) every 6 hours. The orbital parameters and greenhouse gas~~es~~ concentrations have been set to the values of the corresponding model year. The monthly mean sea surface temperature and sea-ice fields from the ERA5 reanalysis have been applied as ocean surface boundary conditions, as well as a mean $\delta^{18}O$ of surface seawater reconstruction from the global gridded data set of ~~(~~LeGrande and Schmidt~~,~~ (2006). As no equivalent data set of the δD composition of

Mis en forme: Police :Gras

seawater exists, the δD of the seawater in any grid cell has been set equal to the related $\delta^{18}O$ composition, multiplied by a factor of 8, in accordance with the observed relation for meteoric water on a global scale (Craig, 1961). The ECHAM6-wiso simulation is described in detail and evaluated ~~in~~ by Cauquoin and Werner (2021). ECHAM6-wiso outputs are given at a 6-hourly resolution. As for the LMDZ-iso model, ~~the~~ Amsterdam Island (58 km^2) is too small to be represented by ECHAM6-wiso.

3. Results

3.1 Data description

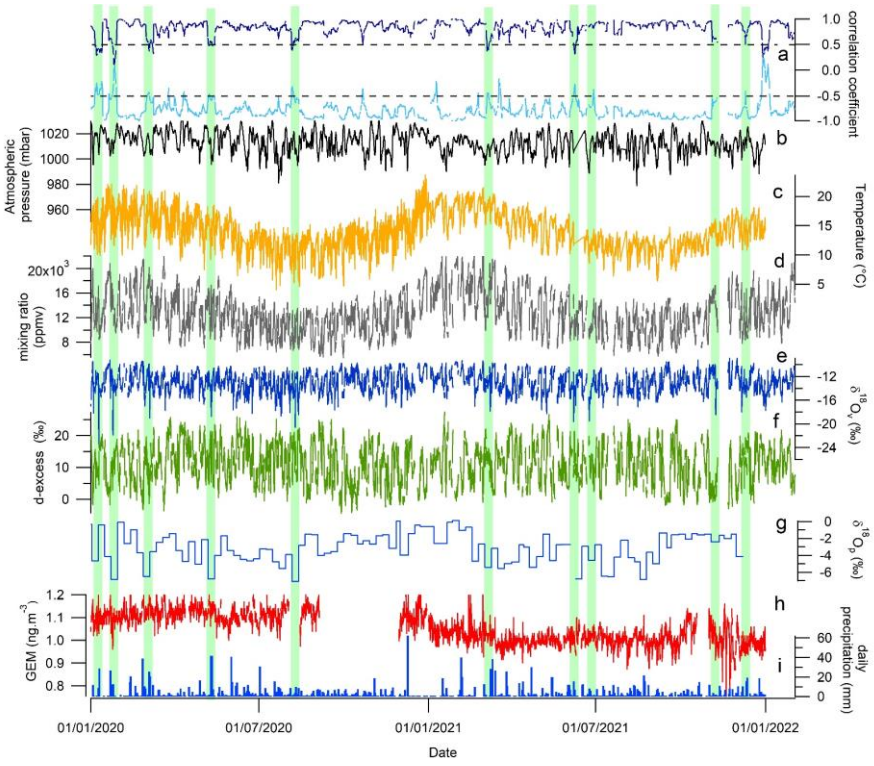

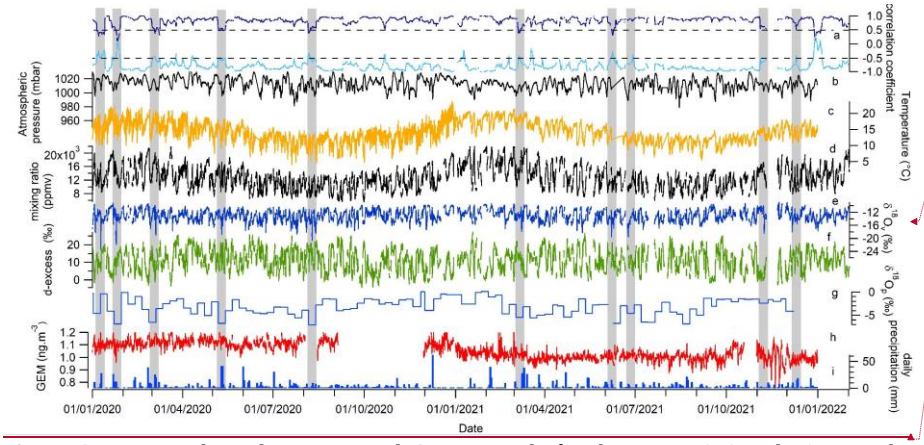

Figure 3 : Meteorological, isotopic and GEM records for the years 2020 and 2021 on the Amsterdam Island : (a) correlation coefficient between ~~water vapor~~ $\delta^{18}O_v$ and mixing ratio (dark blue, top) and between ~~water vapor~~ $\delta^{18}O_v$ and d-excess$_v$ (light blue, bottom) over a moving time window of 8 days, (b) atmospheric pressure (hourly average), (c) atmospheric temperature (hourly average), (d) water vapor mixing ratio (hourly average), (e) $\delta^{18}O_v$ ~~of water vapor~~ (hourly average), (f) d-excess$_v$ ~~of water vapor~~ (hourly average), (g) $\delta^{18}O$ of precipitation sampled on a weekly basis, (h) GEM concentration (hourly average), (i) daily precipitation. The ~~green~~ grey shaded areas~~rectangles~~ indicate the ~~period~~ the negative excursions in $\delta^{18}O_v$ associated with decorrelation between water vapor mixing ratio and $\delta^{18}O_v$ and ~~with (1)~~a correlation coefficient >-0.5 between d-excess$_v$ and $\delta^{18}O_v$ ~~of water vapor and (2) occurrence of a negative excursion in water vapor $\delta^{18}O$.~~

Mis en forme: Corps, Gauche, Interligne : simple

Mis en forme: Police par défaut, Police :

3.1.1 Temporal variability in the meteorological records

As mentioned earlier, there is a clear annual cycle at Amsterdam Island as recorded in the temperature and water vapor mixing ratio for the years 2020 and 2021. The December-February period (austral summer) has the highest temperatures with an average of 15.0°C, while in winter (July-September) the average temperature varies around 10.5°C. In parallel, we do not see clear patterns of a diurnal cycle in the temperature record except for some periods ~~in the temperature records~~ yet with a small amplitude (4-5 °C).

The impact of synoptic events at the scale of a few days is visible in the temperature and water mixing ratio with a covariation of temperature and water vapor mixing ratio and ~~with~~ amplitudes of up to 10°C ~~in temperature~~ and more than 10,000 ppmv~~. in water mixing ratio.~~

3.1.2 Temporal variability in the GEM record

Previous studies clearly showed that AMS is little influenced by anthropogenic sources of ~~Hg~~mercury, and greatly influenced by the ocean surrounding the island (Angot et al., 2014; Hoang et al., 2023; Jiskra et al., 2018; Li et al., 2023; Slemr et al., 2015, 2020~~; Jiskra et al., 2018; Li et al., 2023; Hoang et al., 2023~~). Angot et al., ~~(~~2014~~)~~ reported mean annual GEM concentrations of about 1.03 ± 0.08 ng m^{-3} from 2012 to 2013. These concentrations are ~30% lower than those measured ~~in~~ at remote sites of the northern hemisphere. Over the period 2012 to 2017, Slmer et al. (2020) confirmed that higher GEM concentrations can be found during austral winter. Lower GEM values are generally observed in October and November, as well as in January and February during austral summer. Using this 6-year long data set, mean annual GEM concentration ~~i~~was 1.04 ± 0.07 ng m^{-3} (annual range: 1.014 to 1.080 ng m^{-3}) i.e. very close to the one observed by~~in~~ Angot et al. (2014).

~~During the period (2020-2021) of water vapor isotope measurements in AMS, GEM showed mean annual concentration in the range of 1.11 ± 0.04 ng m^{-3} and 1.00 ± 0.04 ng m^{-3}, for years 2020 and 2021 respectively, slightly higher and lower than the ones observed in previous mentioned studies.~~ Surprisingly, unlike the 2012-2017 data set, GEM presented in this study did not show a significant higher mean concentration during the austral winter months than during the summer months (Figure 3), with consequently no discernible seasonal amplitude of GEM. On a finer timescale, the lack of a clear pattern of GEM seasonal cycle is counterbalanced by days showing abrupt increases or decreases in concentrations. Some of the sudden GEM decreases ~~(until more than 15 % of the concentration in few hours, i.e. up to 0.15-0.20 ng m^{-3} difference)~~ appear concomitant with important negative peaks of several ‰ in ~~water vapor~~ $\delta^{18}O_v$.

3.1.3 Temporal variability of water isotopic composition

The isotopic composition of precipitation ($\delta^{18}O_p$) sampled on a weekly basis displays a quite large variability ($\delta^{18}O_p$ = -3.06 ± 1.75 ‰, n=104) with values slightly higher during austral summer (difference between summer and winter $\delta^{18}O_p$ values is about 2 to 3 ‰) (Figure 3). No significant seasonal variations are observed in the record of d-excess of ~~the~~ precipitation (not shown).

No diurnal cycle can be detected in the $\delta^{18}O_v$ and d-excess$_v$. ~~The annual cycles are also~~An annual cycle is ~~-~~not visible either (1 ‰ difference between summer and winter mean $\delta^{18}O_v$ value while standard deviation of the entire record at 1 h resolution is 1.7 ‰). Only the synoptic scale variability is well expressed in the records of $\delta^{18}O_v$ and d-excess$_v$ with an anticorrelation between both parameters when looking at the 2-year series at hourly resolution (R^2 = 0.61 with R^2 being the coefficient of determination for a linear regression). Moreover, ~~water vapor~~ $\delta^{18}O_v$ is most of the time correlated with water vapor mixing ratio (R^2 = 0.55 for the 2-year series at hourly resolution).

There are a few exceptions to the general correlation between water vapor $\delta^{18}O$ and water vapor mixing ratio as illustrated ~~on~~ in Figure 3. Short periods of a few days are associated with a decrease of the correlation coefficient, R~~,~~ estimated from the correlation between $\delta^{18}O_v$ and q_v (R is calculated continuously from hourly records ~~in 8 consecutive days~~on an 8-day moving window). The periods of low~~decreased~~ R are also often characterized by a negative peak of several ‰ in $\delta^{18}O_v$, which ~~are~~ is not visible in the d-excess$_v$. During these $\delta^{18}O_v$ excursions ~~occurring during cold fronts~~, the general anti-correlation between $\delta^{18}O_v$ and d-excess$_v$ hence also breaks down. Our study mostly focuses on the 11 most prominent abrupt events highlighted in the ~~by the water vapor~~ $\delta^{18}O_v$ record (only 10 visible on Figure 3 because of the scale). The 11 most abrupt events occurring when correlation coefficient R between $\delta^{18}O_v$ and d-excess$_v$ is larger than -0.5 are associated with $\delta^{18}O_v$ negative excursion larger than 3 ‰ (at 6h resolution) over a period of less than 24 h, the length of the event being measured between the mid-slopes of the decrease and subsequent increase of the $\delta^{18}O_v$. The 11 selected negative excursions occur at a rate larger than -0.5‰ h^{-1} and the $\delta^{18}O_v$ increase at the end of each excursion has an amplitude larger than half the amplitude of the corresponding initial decrease.

Mis en forme: Exposant

Mis en forme: Indice

Mis en forme: Exposant

3.2 Model-data comparison

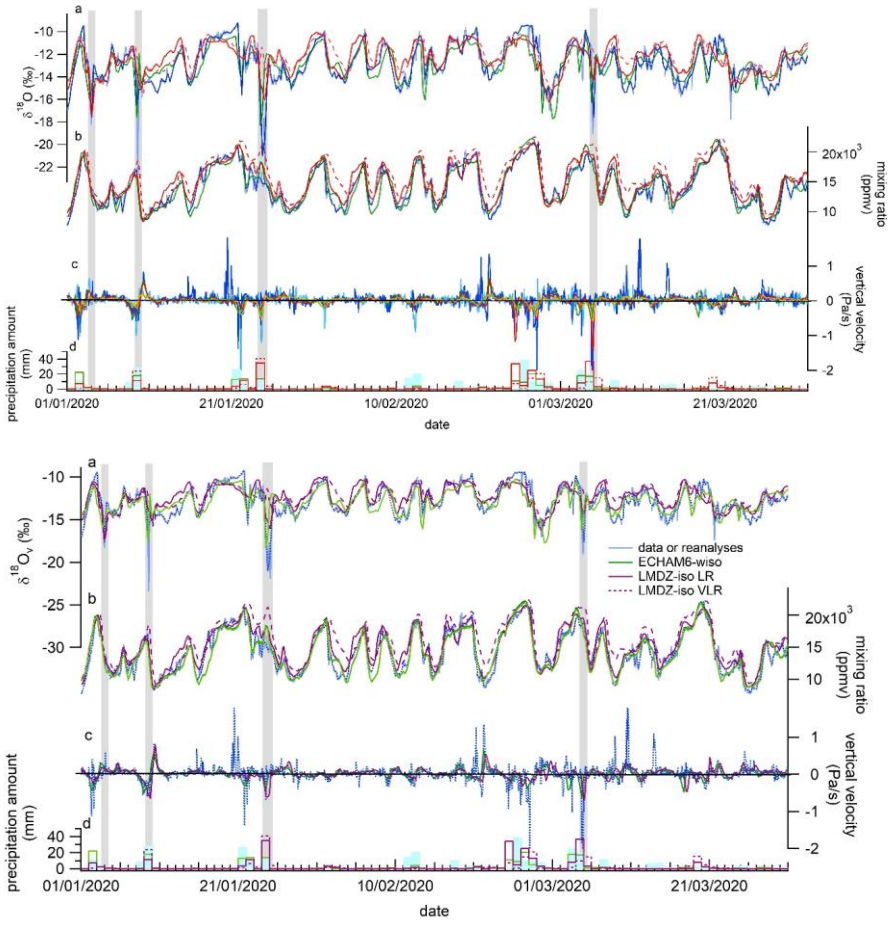

Figure 4: Model-measurement comparison (January – March 2020): a- $\delta^{18}O_v$ (light blue for data on hourly average, dotted dark blue for data resampled at a 6-hour resolution); b- water vapor mixing ratio from our data set; c- vertical velocity; d- Precipitation amount. The grey shaded areas highlight the negative $\delta^{18}O_v$ excursions as defined in 3.1.3 (note that in this figure the excursions of the 3rd and 9th of January 2020 are distinct while the distinction could not be done on Figure 3 because of the scale).

~~**Figure 4**: Data-model comparison (January – March 2020) : water vapor $\delta^{18}O$ from our data set (light blue on hourly average, dark blue resampled at a 6-hour resolution), the ECHAM6-wiso model (green, surface level, 6h resolution) and the LMDZ-iso model (red, surface level, 3h resolution) at very low resolution (VLR, dashed line) and at low resolution (LR, solid line) (a) ; mixing ratio from our data set (light blue on hourly average, dark blue resampled at a 6~~

Mis en forme: Police :(Par défaut) Times New Roman, 12 pt, Gras, Soulignement , Couleur de police : Automatique

Mis en forme: Police :(Par défaut) Times New Roman, 12 pt, Couleur de police : Automatique

Mis en forme: Police :12 pt, Couleur de police : Automatique

Mis en forme: Police :(Par défaut) Times New Roman, 12 pt, Couleur de police : Automatique

Mis en forme: Police :(Par défaut) Times New Roman, 12 pt, Couleur de police : Automatique

Mis en forme: Police :12 pt

Mis en forme: Police :(Par défaut) Times New Roman, 12 pt, Couleur de police : Automatique

Mis en forme: Police :12 pt, Couleur de police : Automatique

Mis en forme: Police :(Par défaut) Times New Roman, 12 pt, Couleur de police : Automatique

Mis en forme: Police :12 pt

Mis en forme: Police :(Par défaut) Times New Roman, 12 pt, Couleur de police : Automatique

Mis en forme: Police :(Par défaut) Times New Roman, 12 pt, Couleur de police : Automatique

~~hours resolution), the ECHAM6-wiso model (green, surface level, 6h resolution) and the LMDZ-iso model (red, surface level, 3h resolution, dashed line for VLR and solid line for LR) (b) ; vertical velocity from the ERA5 reanalyses (500 hPa, blue, 850 hPa, light blue), from the ECHAM6-wiso model (500 hPa, green, 850 hPa, light green), from the LMDZ-iso model at LR (500 hPa, red, 850 hPa, orange) (c) ; Precipitation amount from the meteorological record in light blue, from the ECHAM6-wiso model in green and from the LMDZ-iso model in red (dashed line VLR and solid line LR) (d). The grey rectangles highlight the negative $\delta^{18}O$ excursions (note that in this figure the excursions of the 3rd and 9th of January 2020 are distinct while the distinction could not be done on Figure 3 because of the scale).~~

We selected a 3-month period (January to March 2020) for the comparison between our ~~set of data~~dataset and the outputs of the ECHAM6-wiso and LMDZ-iso models. This period has been selected for display because it encompasses 4 out the 11 negative excursions of $\delta^{18}O_v$, but the extended comparison over the whole 2 years period is displayed ~~on~~ in Figure ~~S1~~A1. There is an overall agreement between the measured and modelled ~~water vapor~~ $\delta^{18}O_v$ and water vapor mixing ratio (Figure 4). The best agreement over the 3-month series is obtained with the ECHAM6-wiso and LMDZ-iso (LR) models (R^2 = 0.59 – 0.6 and 0.87 - 0.90 respectively for $\delta^{18}O_v$ and water vapor mixing ratio series) while a slightly less good agreement is observed with the VLR simulation of the LMDZ-iso model (R^2 = 0.49 and 0.79 respectively for $\delta^{18}O_v$ and water vapor mixing ratio series). The same observation can be done on the entire ~~two~~2-year time series. We also compare the precipitation amount modelled by ECHAM6-wiso and LMDZ-iso to the precipitation amount measured by the MeteoFrance weather station. The correlation between modeled and measured precipitation is close to zero for LMDZ-iso (R^2 = 0.08 – 0.13 for VLR - LR) while there is a better ~~and in general, the~~ agreement when comparing ~~with~~ measured precipitation amount to outputs of ~~is better for~~ ECHAM6-wiso (R^2 = 0.45). ~~than for LMDZ-iso (R^2 = 0.08 – 0.13 for VLR - LR)~~. Finally, when focusing on the ~~4~~ short term negative $\delta^{18}O_v$ excursions ~~of the water vapor $\delta^{18}O$~~ (~~grey rectangles in~~ Figures ~~5~~4 and A1), they are in general more strongly expressed in the measurement time~~data~~ series than in the model series. Part of this disagreement can be explained by the fact that the ~~which is only partly due to the hourly resolution of the~~ $\delta^{18}O_v$ record has a higher temporal resolution (1h) than the ~~compared to the 3h and 6h resolution of the~~ model outputs (~~outputs of the~~ 3h for LMDZ-iso and 6h for ECHAM6-wiso~~) models respectively~~. However, when interpolating the $\delta^{18}O_v$ record at a 6h resolution (dotted dark blue), the negative excursions are still clearly visible while not

captured by the LMDZ-iso model ~~(~~Figure ~~4 red dashed and solid lines on panel c~~4 and Table 1~~ 9th column))~~. When looking at the whole ~~two~~2-year series, the LMDZ-iso VLR simulation fails to reproduce most of these $\delta^{18}O_v$ excursions (only the negative excursion of ~~the~~ 3rd ~~of~~ January, 2020 is reproduced) while the ECHAM6-wiso model is able to capture all the $\delta^{18}O_v$ excursions. The LMDZ-iso LR simulation produces a negative $\delta^{18}O_v$ excursion over many events with a significantly lesser amplitude than ~~but significantly less expressed than~~ in the data and in the ECHAM6-wiso model (Table 1).

4. Discussion

The most remarkable pattern from this ~~two~~2-year series is the succession of short negative excursions of $\delta^{18}O_v$ associated with decorrelation between $\delta^{18}O_v$ and humidity, $\delta^{18}O_v$ and d-excess$_v$, and which are highlighted with ~~green~~ grey ~~rectangles~~ shaded areas in Figure 3, detailed in Figures 5 and A2 and referenced in Table 1. ~~They~~ These negative $\delta^{18}O_v$ excursions always occurred during low pressure periods (atmospheric pressure below 1005 mbar) and~~,~~ we observe the presence of a cold front within a distance of 100 km around Amsterdam Island in a 48h period covering the time of the event (supplementary material Figure S1). The focus on the first three months of the series presented ~~on~~ in Figure 4 shows that these events are captured by ECHAM6-wiso at 0.9° resolution, but not systematically by LMDZ-iso at 2x1.67° and even less by LMDZ-iso at 3.75x1.9° resolution. Such mismatch makes the understanding of the processes at play during these events particularly important to investigate to further improve the performances of atmospheric general circulation models equipped with water isotopes. ~~Such mismatch makes the understanding of the processes at play during these events particularly important to test and improve the performances of atmospheric general circulation models equipped with water isotopes~~.

Mis en forme: Non souligné

Mis en forme: Police :Symbol

Mis en forme: Exposant

Mis en forme: Indice

Mis en forme: Couleur de police : Automatique

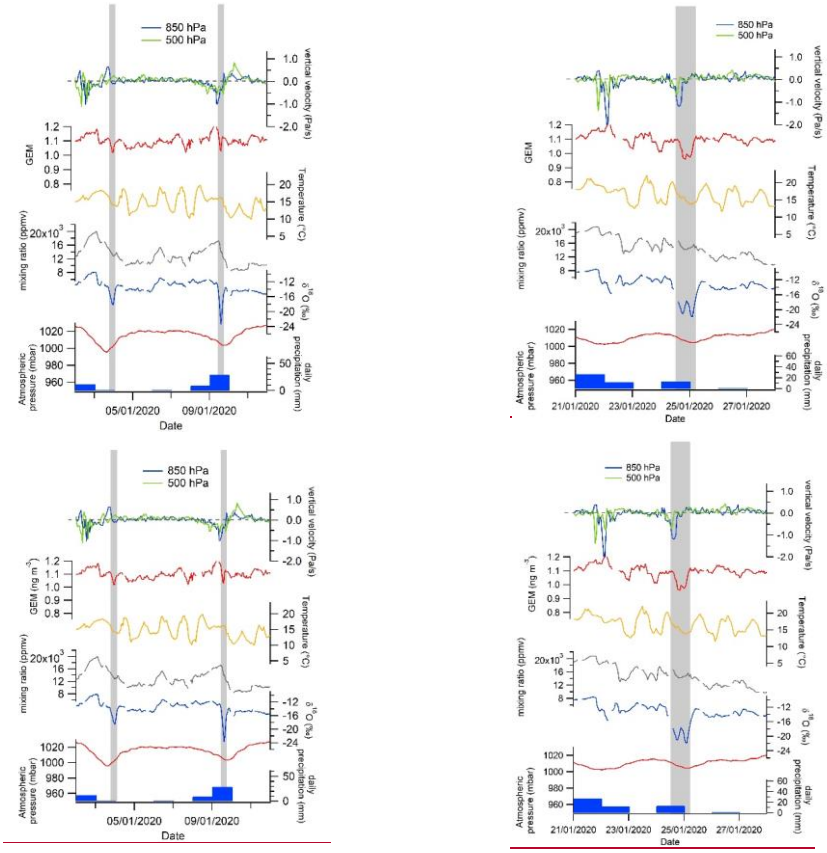

548

549 **Figure 5-:** Evolution of GEM, ~~water vapor~~ $\delta^{18}O_v$, water vapor mixing ratio, meteorological
550 parameters (surface temperature, surface atmospheric pressure, daily precipitation) measured
551 by the MeteoFrance weather station and vertical velocity from the ERA5 reanalyses at 500 and
552 850 hPa over the three isotopic excursions of January 2020 identified on Figure 4. A focus on
553 the other excursions is provided in Figure A2.

554

555 **Table 1**: List of the 11~~cold front~~ events associated with both loss of correlation between $\delta^{18}O_v$
556 and q_v, $\delta^{18}O_v$ and d-excess$_v$ and negative excursions of $\delta^{18}O_v$ over 2020-2021. ~~The length of~~
557 ~~the event is estimated from the time difference between the mid-slope of the $\delta^{18}O_v$ decrease at~~
558 ~~the beginning of the event and the mid-slope of the $\delta^{18}O_v$ increase at the end of the event.~~ The
559 amplitude of the negative $\delta^{18}O_v$ anomaly is calculated from ~~calculated between the average~~

~~$\delta^{18}O_v$ level 24h before and 24h after the excursion and~~ the minimum of $\delta^{18}O_v$ on the record at hourly resolution (at 6h resolution). .When the calculated amplitude is smaller than 1 ‰, we indicate only "-". When the vertical velocity is between -0.25 and 0.25 Pa/s, we indicate "~0".

Date of the event	Negative excursion of GEM	Low pressure (< 1005 mbar)	Rain	Relative Humidity at the surface	vertical velocity from reanalyses (850 hPa)	vertical velocity from reanalyses (500 hPa)	Lenth of the event (hours)	amplitude of the $\delta^{18}O$ peak in the data (‰)	amplitude of the $\delta^{18}O$ peak in ECHAM-wiso (‰)	amplitude of the $\delta^{18}O$ peak in LMDZ-iso VLR (‰)	amplitude of the $\delta^{18}O$ peak in LMDZ-iso LR (‰)
06/12/2021	Yes	Yes	Yes	82%	~0	up	3h	-6 (-5)	-2.3	-	-2
08/11/2021	Yes	Yes	No	85%	~0	~0	17h	-5.5 (-5.5)	-5	-	-4
23/06/2021	No	Yes	Yes	75%	~0	~0	10h	-5.5 (-5.4)	-6	-	-
07/06/2021	No	Yes	Yes	80%	up	~0	9h	-6.5 (-5.8)	-5.8	-	-2
08/03/2021	Yes	Yes	Yes	89%	down	up	20h	-6 (-6)	-4	-	-
09/08/2020	No data	Yes	Yes	87%	down	up	8h	-8 (-6)	-7	-	-2
10/05/2020	Small	Yes	Yes	95%	down	down	14h	-4.9 (-4)	-3	-	-3
04/03/2020	No data	Yes	Yes	98%	Up	Up	9h	-6.1 (-5.3)	-5	-	-
24/01/2020 (double peak)	Yes	Yes	Yes	93% and 90%	1st peak up and 2nd peak down	1st peak up and 2nd peak down	17h	-7.8 (-7.5)	-4.5	-	-3.5
09/01/2020	Yes	Yes	Yes	94%	up	up	4h	-9 (-4)	-5	-	-
03/01/2020	Yes	Yes	No	90%	down	~0	6h	-2.8 (-2.5)	-2.4	-3	-3.5

Date of the event	Negative excursion of GEM	Low pressure (< 1005 mbar)	Rain	Relative Humidity at the surface (at minimum $\delta^{18}O_v$)	vertical velocity from reanalyses (850 hPa)	vertical velocity from reanalyses (500 hPa)	Length of the event (hours)	amplitude of the $\delta^{18}O_v$ peak in the data (‰)	amplitude of the $\delta^{18}O$ peak in ECHAM-wiso (‰)	amplitude of the $\delta^{18}O$ peak in LMDZ-iso VLR (‰)	amplitude of the $\delta^{18}O$ peak in LMDZ-iso LR (‰)
06/12/2021	Yes	Yes	Yes	82%	~0	up	3h	-6 (-5)	-2.3	-	-2
08/11/2021	Yes	Yes	No	85%	~0	~0	17h	-5.5 (-5.5)	-5	-	-4
23/06/2021	No	Yes	Yes	75%	~0	~0	10h	-5.5 (-5.4)	-6	-	-
07/06/2021	No	Yes	Yes	80%	up	~0	9h	-6.5 (-5.8)	-5.8	-	-2
08/03/2021	Yes	Yes	Yes	89%	down	up	20h	-6 (-6)	-4	-	-
09/08/2020	No data	Yes	Yes	87%	down	up	8h	-8 (-6)	-7	-	-2
10/05/2020	Small	Yes	Yes	95%	down	down	14h	-4.9 (-4)	-3	-	-3
04/03/2020	No data	Yes	Yes	98%	up	up	9h	-6.1 (-5.3)	-5	-	-
24/01/2020 (double peak)	Yes	Yes	Yes	93% and 90%	1st peak up and 2nd peak down	1st peak up and 2nd peak down	17h	-7.8 (-7.5)	-4.5	-	-3.5
09/01/2020	Yes	Yes	Yes	94%	up	up	4h	-9 (-4)	-5	-	-
03/01/2020	Yes	Yes	No	90%	down	~0	6h	-2.8 (-2.5)	-2.4	-3	-3.5

Several hypotheses can be proposed to explain the negative excursions of ~~water vapor~~ $\delta^{18}O_v$ ~~during cold front periods~~. The beginning of these excursions is associated with a decrease of the water vapor mixing ratio and ~~they~~ occurs in most cases ~~(but not always)~~ during a precipitation event (Table 1). These events share similarities with ~~the~~ negative $\delta^{18}O_v$ and $\delta^{18}O_p$ short events previously observed in temperate regions during a cold front passage (e.g. Aemisegger et al., 2015). Three possible processes at play to explain such events have~~were~~ already been listed in previous studies (e.g. Dütsch et al., 2016) (i) local interaction between the vapor and the rain droplets (rain equilibration and rain evaporation), (ii) vertical subsidence of water vapor with depleted isotopic composition, or (iii) horizontal advection through the arrival of a cold front. We ~~first~~ explore below how we can gain information on the different processes ~~listed above from~~using our data set, back trajectories and model-data comparison.

4.1 $\delta^{18}O_v$ vs q_v relationship

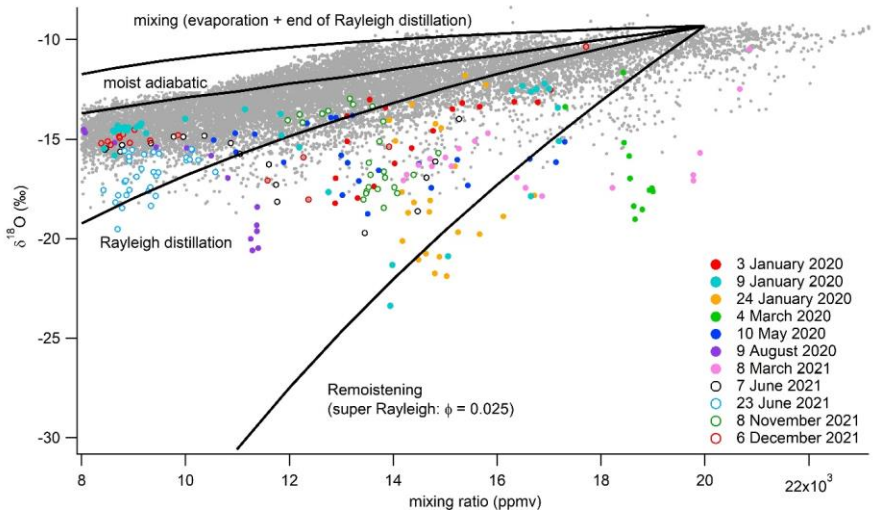

Figure 6: Relative ~~E~~evolution of q_v ~~the mixing ratio~~ and $\delta^{18}O_v$ ~~isotopic composition of water vapor~~ for the different events (colors according to the date as explained ~~o~~in the graph) and for the entire 2 years records (grey). The solid lines are theoretical lines ~~inspired~~ whose equations are detailed in~~from~~ ~~(~~Noone ~~,(~~2012) for different processes (remoistening associated with exchange between rain and water vapor; Rayleigh distillation assuming that all formed condensation is removed from the cloud; moist adiabatic process assuming that liquid condensation stays in the cloud with the water vapor; mixing of water vapor from ocean evaporation around Amsterdam Island and water vapor from the end of the Rayleigh

Mis en forme: Police :Gras
Mis en forme: Police :Symbol, Gras
Mis en forme: Police :Gras, Exposant
Mis en forme: Police :Gras
Mis en forme: Police :Gras, Indice
Mis en forme: Police :Gras
Mis en forme: Police :Gras, Indice
Mis en forme: Police :Gras
Mis en forme: Police :Gras
Mis en forme: Indice

distillation, i.e. high altitude water vapor). The water vapor for the calculation of Rayleigh distillation and for the evaporation above the ocean has a $q_{v,0}$ ~~mixing ratio~~ of 20,000 ppmv and a $\delta^{18}O_{v,0}$ of -9.3 ‰. The vapor at the end of the distillation line was taken with a water vapor mixing ratio of 1,000 ppmv and a $\delta^{18}O_v$ of -40 ‰.

~~We first explore how we can gain information on the different processes listed above from our data set.~~ First, to test the hypothesis of vapor-droplet interactions, we looked at the $\delta^{18}O_v$ vs q_v distribution following the approach already used by Guilpart et al. (2017) (Figure 6). We acknowledge that our approach is crude and should be taken as a first order approach since we can only look at the water vapor $\delta^{18}O_v$ vs q_v distribution in the surface layer using adapted boundary conditions while it may be more relevant to look at this relationship in the free troposphere. In general, the $\delta^{18}O_v$ vs q_v evolution lies on a curve which can be explained by condensation processes (Rayleigh distillation or reversible moist adiabatic process). However, for the 11 events highlighted above, the water vapor $\delta^{18}O_v$ vs q_v evolution follows an evolution ~~characteristic of remoistening processes, i.e. a curve~~ standing below the curve of the $\delta^{18}O_v$ vs q_v evolution observed for the rest of the series. Even if the water vapor $\delta^{18}O_v$ vs q_v evolution is rather steep, there is some resemblance with the idealized theoretical curve for remoistening initially calculated for the free troposphere (Noone, 2012) and adapted here with initial conditions corresponding to the surface water vapor isotopic composition. Remoistening is described through a modification of the equilibrium fractionation coefficient between water vapor and rain (α_e) so that the effective fractionation factor is $\alpha=(1+\phi)\times\alpha_e$, ϕ being the degree to which α deviates from equilibrium. This effective fractionation coefficient is then introduced in the Rayleigh distillation equation to deduce the link between $\delta^{18}O_v$ and mixing ratio as:

$$\delta^{18}O_v-\delta^{18}O_{v,0})=(\alpha-1)*\ln(q_v/q_{v,0}) \quad \text{(Eq 8)}$$

Despite the simplicity of our approach, the fact that the water vapor $\delta^{18}O_v$ vs q_v evolution lies below the idealized curve for condensation processes supports the depleting effect of vapor-rain interactions for our negative water vapor $\delta^{18}O_v$ excursions (Noone, 2012; Worden et al., 2007). ~~, which demonstrates the depleting effect of vapor-rain interactions (Worden et al., 2007; Noone, 2012). Since r~~Surface relative humidity remain~~is~~ relatively high during these events (values given in Table 1 compared to a mean value of 77 %)~~,~~ which favors ~~it more likely reflects~~ rain-vapor diffusive exchanges ~~than rain evaporation~~. Such interpretation is also supported by the stable d-excess$_v$ during these events.

Mis en forme: Indice
Mis en forme: Police :Symbol
Mis en forme: Exposant
Mis en forme: Indice
Mis en forme: Indice
Mis en forme: Police :Symbol
Mis en forme: Indice
Mis en forme: Police :Symbol
Mis en forme: Police :Symbol
Mis en forme: Police :Symbol
Mis en forme: Indice
Mis en forme: Police :Symbol
Mis en forme: Police :Symbol
Mis en forme: Exposant
Mis en forme: Indice
Mis en forme: Police :Symbol
Mis en forme: Retrait : Gauche : 1.25 cm, Première ligne : 1.25 cm
Mis en forme: Police :(Par défaut) Times New Roman, Exposant
Mis en forme: Police :(Par défaut) Times New Roman
Mis en forme: Indice
Mis en forme: Indice
Mis en forme: Police :Symbol
Mis en forme: Indice

4.2 $\delta^{18}O_v$ vs GEM relationship

Second, to test the hypothesis~~,~~ of subsidence of air from higher altitude, GEM is used. Indeed, aircraft measurements as well as model simulations demonstrated that the upper troposphere/lower stratosphere ~~(UTLS)~~ is depleted in GEM and enriched in species composed of reactive gaseous mercury and particulate bound mercury (Lyman and Jaffe, 2012; Murphy et al., 2006; Sillman et al., 2007; Swartzendruber et al., 2006, 2008; ~~Sillman et al., 2007;~~ Talbot et al., 2007, 2008~~; Lyman and Jaffe, 2012~~). This leads to lower GEM concentrations than those usually observed when the lowest atmosphere layer is only under marine influence (Angot et al., 2014; Lindberg et al., 2007~~; Angot et al., 2014~~). The fact that GEM negative excursions are observed in phase with negative $\delta^{18}O_v$ excursions in most of the events (~~7~~ 6 events on a total of 9 events with GEM data, cf Figure 5 and A2, Table 1) suggests that vertical subsidence of water vapor, $\delta^{18}O$-depleted by Rayleigh distillation and/or rain-vapor interactions, can have an influence on the observed excursions of $\delta^{18}O_v$, in agreement with the conclusion of Dütsch et al. (2016).

4.3 Back trajectories information

To further explore the processes leading to the decoupling of humidity and $\delta^{18}O_v$ as well as sharp negative excursions of $\delta^{18}O_v$ during the 11 events identified here, we also use information from the ERA5 reanalyses. In particular, the influence of atmospheric circulation (vertical and horizontal advection) and moisture origin can be studied through back trajectories. The back trajectories, presented here for 3 events (~~see some examples in SI,~~ Figures 7, A3 and A4~~S2 and S3~~), confirm the information from wind directions that there is no systematic change in the horizontal origin of the trajectories for the different events. ~~On the contrary, back trajectories clearly indicate a strong subsidence o~~No systematic pattern is identified either in the vertical advection even if we note that ~~ver some events, in particular~~ for the event of ~~the 3rd of~~ January 3rd, ~~:~~ the average~~maximum~~ altitude of the envelope of the 5-day back trajectories increases ~~from 5,000 to 8,000 m~~ when comparing the situation before the excursion and the situation ~~during~~ when the most negative ~~water vapor~~ $\delta^{18}O_v$ values are reached. This observation may support ~~,~~ ~~hence confirming~~ the occurrence of air subsidence as indicated by the GEM record for this particular event (Figure ~~S2~~5). ~~A less clear but similar situation is observed for the anomaly of the 24th of January 2020 which is associated with an increase of the maximum altitude of the back trajectories from 4,000 to 6,000 m when comparing the situation before the excursion and~~

Mis en forme: Police :Gras
Mis en forme: Police :Symbol, Gras
Mis en forme: Police :Gras, Exposant
Mis en forme: Police :Gras
Mis en forme: Police :Gras, Indice
Mis en forme: Police :Gras
Mis en forme: Police :Gras
Mis en forme: Exposant
Mis en forme: Indice

~~the situation corresponding to the most negative water vapor $\delta^{18}O$ value. Back trajectories are however not supporting systematic subsidence for other cases (e.g. event of the 9th of January, Figure S3).~~

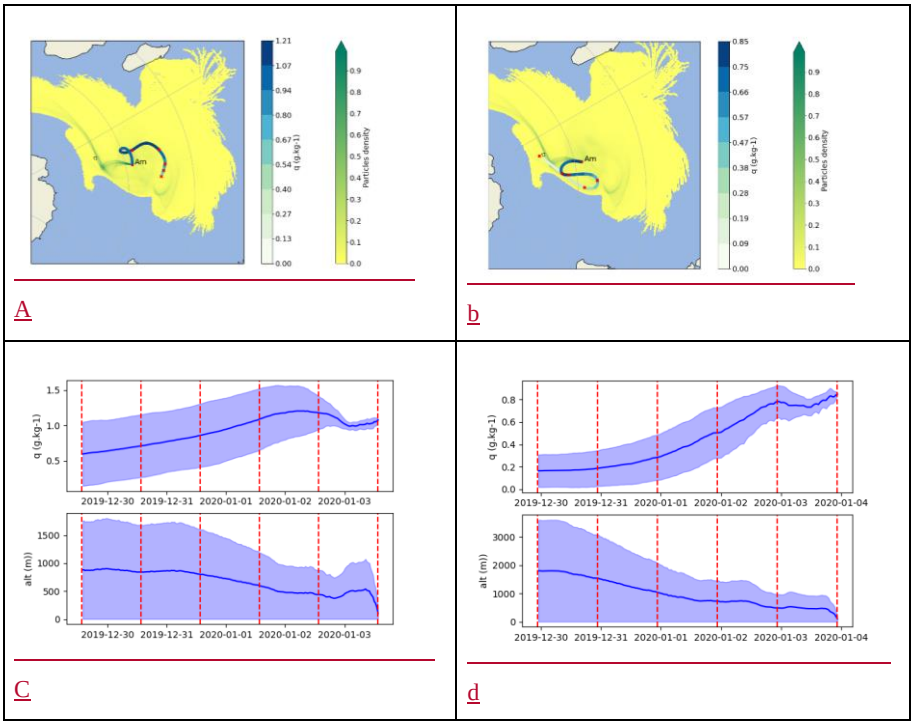

Figure 7 : FLEXPART footprints of 5-day back trajectories for the event of the 3rd-4th of January. (a) Latitude-longitude projection of the FLEXPART back trajectory footprints for January 3rd 2020 at 13h30. The yellow to green colors on each grid point of these projections represent the density of particles. The white to blue colors indicate the water vapor mixing ratio along the humidity-weighted average back trajectory. Each red point indicates the location of the average back trajectory for each of the 5 days before the date of the considered event. (b) Same as a for January 3rd 2020 at 22h30. (c) Top shows the evolution of the water vapor mixing ratio of the back trajectories for January 3rd 2020 at 13h30; bottom shows the altitude evolution of the back trajectory for January 3rd 2020 at 13h30. (d) same as (c) for January 3rd 2020 at 22h30.

Mis en forme: Couleur de police : Automatique
Mis en forme: Couleur de police : Automatique
Mis en forme: Interligne : 1.5 ligne
Mis en forme: Couleur de police : Automatique, Exposant
Mis en forme: Couleur de police : Automatique, Exposant
Mis en forme: Couleur de police : Automatique
Mis en forme: Couleur de police : Automatique
Mis en forme: Exposant
Mis en forme: Couleur de police : Automatique
Mis en forme: Couleur de police : Automatique
Mis en forme: Couleur de police : Automatique
Mis en forme: Couleur de police : Automatique
Mis en forme: Couleur de police : Automatique
Mis en forme: Exposant
Mis en forme: Couleur de police : Automatique
Mis en forme: Couleur de police : Automatique
Mis en forme: Couleur de police : Automatique
Mis en forme: Exposant
Mis en forme: Couleur de police : Automatique
Mis en forme: Exposant
Mis en forme: Couleur de police : Automatique
Mis en forme: Couleur de police : Automatique
Mis en forme: Exposant
Mis en forme: Couleur de police : Automatique

The subsidence over the different events can ~~also directly~~better be studied from~~followed on~~ the vertical velocity from the ERA5 reanalyses (Figure 4 and A1). Subsidence (positive vertical velocity) is not systematically associated with negative $\delta^{18}O_v$ excursions: subsidence at either 850 hPa or 500 hPa is observed only for 5 events over 11 (Table 1). In 4 cases, there is rather an ascending movement of the ~~atmosphere~~ atmospheric air associated with the rain event. In the other cases, there is no clear vertical movement. However, we note that when negative $\delta^{18}O_v$ excursions are not concomitant with subsidence, they occur right after an ascending movement and are generally followed by subsidence (Figures ~~S1~~A1 and A2).

~~The effect of change in horizontal air mass origin is difficult to study from our data. There is no evidence for changes in the horizontal advection of air over the 11 particular events from the observation of wind direction around these cold front events. The back trajectories permit to look at a possible change of horizontal advection higher in the atmosphere. Again, no clear change of horizontal advection at higher altitude is observed for the 11 events associated with a sharp decrease of the $\delta^{18}O_v$.~~

4.4 Model – data comparison and atmospheric dynamic

With the information gathered above, both subsidence and isotopic depletion associated with rain occurrence and further interaction between droplets and water vapor can explain the negative excursions of $\delta^{18}O_v$. We note however that the data gathered so far do not permit to provide a simple and unique explanation. Neither subsidence nor rain systematically occurred for each of the $\delta^{18}O_v$ excursion. Still, the fact that at least ECHAM6-wiso is able to reproduce every negative $\delta^{18}O_v$ excursion~~s~~ (whether they are associated or not with subsidence or rain-water vapor reequilibration) shows that not only the ~~atmospheric circulation~~ patterns of atmospheric water cycle are correctly reproduced (a validation which can also be performed using humidity and precipitation data) ~~and~~ but also that the isotopic processes are correctly implemented in this model. Such abrupt $\delta^{18}O_v$ events can hence be used as a test bed of the performances of water isotopes enabled general circulation models~~ equipped with water isotopes~~.

To ~~better understand why~~further explore the $\delta^{18}O_v$ data-model~~s~~ comparison and associated processes~~ are less able to reproduce the $\delta^{18}O_v$ excursions at coarser resolution~~, we compare the performances of the ECHAM6-wiso and the LMDZ-iso models over the first months of 2020 in terms of atmospheric dynamics (~~the whole series is displayed in SOM~~Figures 4 and A1). First and as expected because of the nudging, the two models reproduce rather well the

Mis en forme: Police :Gras

evolution of the vertical velocity of~~from t~~ the ERA5 reanalyses with a stronger ascent for the model predicting the strongest precipitation amount (e.g. LMDZ-iso for ~~24th of~~ January 24th 2020). The event of ~~the 3rd of~~ January 3rd is the only one reproduced by both ECHAM6-wiso and the two versions of the LMDZ-iso model: the three simulations show a clear subsidence over the isotopic event and a clear negative $\delta^{18}O_v$ excursion ~~(Figure 4)~~. For the other events, neither LMDZ-iso nor ECHAM6-wiso show a clear signal of subsidence neither at 500 nor at 850 hPa (Figures 4 and A1). However, the horizontal distribution of vertical velocity obtained with ECHAM6-wiso and LMDZ-iso are significantly different (Figure ~~7~~ 8 for the event of the 9th of January, supplementary material Figures S2 and S3~~Figures S5~~ for the other events). While the LMDZ-iso modelled vertical velocity displays a rather strong homogeneity on the vertical axis, ECHAM6-wiso modelled vertical velocity highlights subsidence of air below the ascending column at the exact location of the negative $\delta^{18}O_v$ anomaly (Figure ~~7c~~8c). This subsidence of depleted $\delta^{18}O_v$ below the ascending column is responsible for the sharp negative $\delta^{18}O_v$ excursion in the ECHAM6-wiso model. The fact that subsidence of air occurs just below uplifted air, at the limit between ascendance and subsidence (Figure 8~~7~~j and Supplementary Material Figure S4), permits to reconcile the GEM data suggesting subsidence and the sign of the vertical velocity of the ERA5 reanalyses at Amsterdam Island. ~~We propose that the reason why t~~Since the isotope implementation was done similarly in the two models, the reason why the LMDZ-iso model does not reproduce the water isotopic anomaly is its too coarse resolution as also supported by the comparison between performances of ~~. Indeed, Table 1 and Figure 4 show that for the event of the 24th of January,~~ the LMDZ-iso model at low resolution ~~is able to reproduce the isotopic anomaly while the LMDZ-iso model at~~and very low resolution ~~fails~~for the event of the 24th of January (Table 1 and Figure 4). As already pointed by Ryan et al. (2000), ~~A~~a fine resolution is necessary to correctly simulate front dynamics and we extend this result here to~~capture the details of~~ the high resolution temporal ~~spatial~~ patterns of surface ~~the vertical velocity and~~ $\delta^{18}O_v$. ~~Similar observations can be done on other events as shown in the SI (Figures S5 to S11).~~

4.5 Synthesis

Figure ~~8~~ 9 summarizes the proposed mechanism for negative $\delta^{18}O_v$ excursions as inferred from our data – model comparison when there is a clear rain event. A rain event is associated with a strong ascending column in which $\delta^{18}O_v$ is depleted by progressive precipitation during the ascent and by interaction between rain and water vapor. This ascending column is coupled to

Mis en forme: Exposant

Mis en forme: Exposant

Mis en forme: Police :Symbol

Mis en forme: Police :Gras

the subsidence of $\delta^{18}O_v$ depleted air at the rear of the event, which is pushed toward Amsterdam Island through a south west advection of cold air.

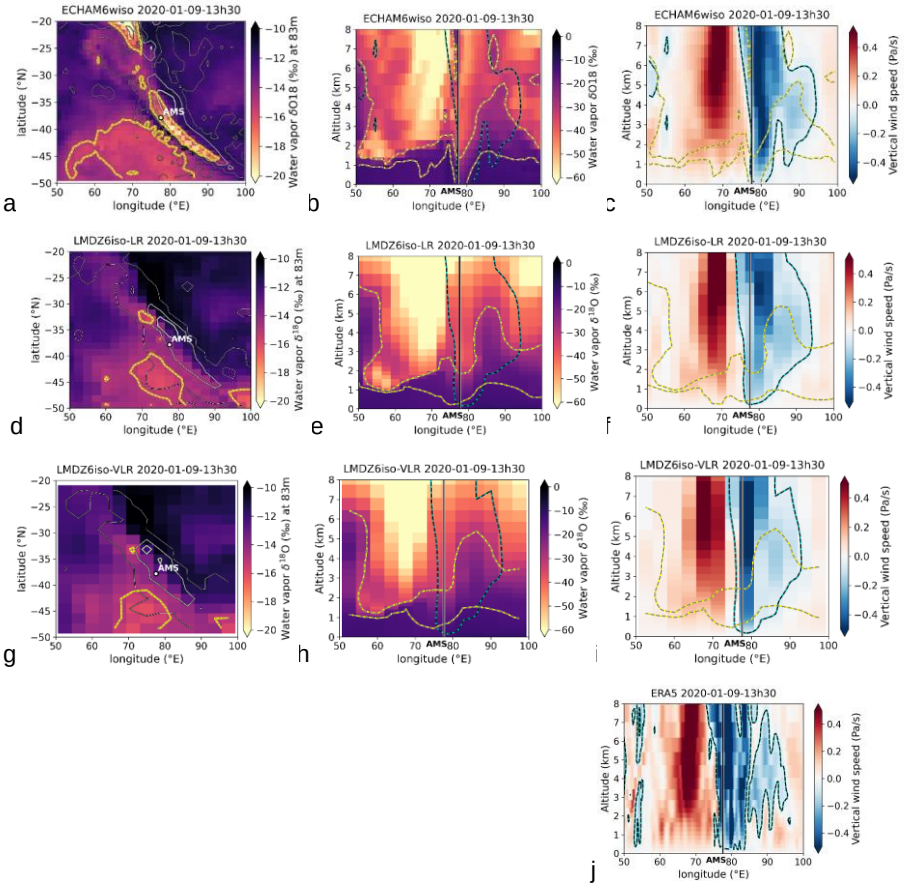

Figure 7~~8~~: Pattern~~Evolution~~ of the modelled $\delta^{18}O_v$ and vertical velocity for ~~over~~ the event of ~~the 9th of~~ January 9th 2020. (a) low level (~83 m) contourplot of $\delta^{18}O_v$ ~~io~~n a latitude vs longitude plot, the yellow line indicates the -15‰ level and grey contours indicate precipitation contours at 0.5, 10, and 50 mm day^{-1} (thin, medium and thick lines respectively); (b) $\delta^{18}O_v$ evolution ~~io~~n an altitude vs longitude plot, the yellow lines indicate the $\delta^{18}O_v$ levels at -30 and -15 ‰, the blue one plots the contour of –0.05 Pa s^{-1} vertical velocity (ascendance) and the vertical black line denotes Amsterdam Island longit~~atit~~ude; (c) vertical velocity ~~evolution o~~in an altitude vs

Mis en forme: Police :Non Gras

Mis en forme: Exposant

longitude plot with similar lines as in (b) ; (a), (b) and (c) are drawn using outputs of the ECHAM6-wiso model ; (d), (e) and (f) are the same as (a), (b) and (c) but obtained from the LMDZ-iso model at low resolution (LR) ; (g), (h) and (i) are the same as (a), (b) and (c) but obtained from the LMDZ-iso model at very low resolution (VLR); (j) shows the vertical velocity ~~i~~n an altitude vs longitude plot from ERA5.

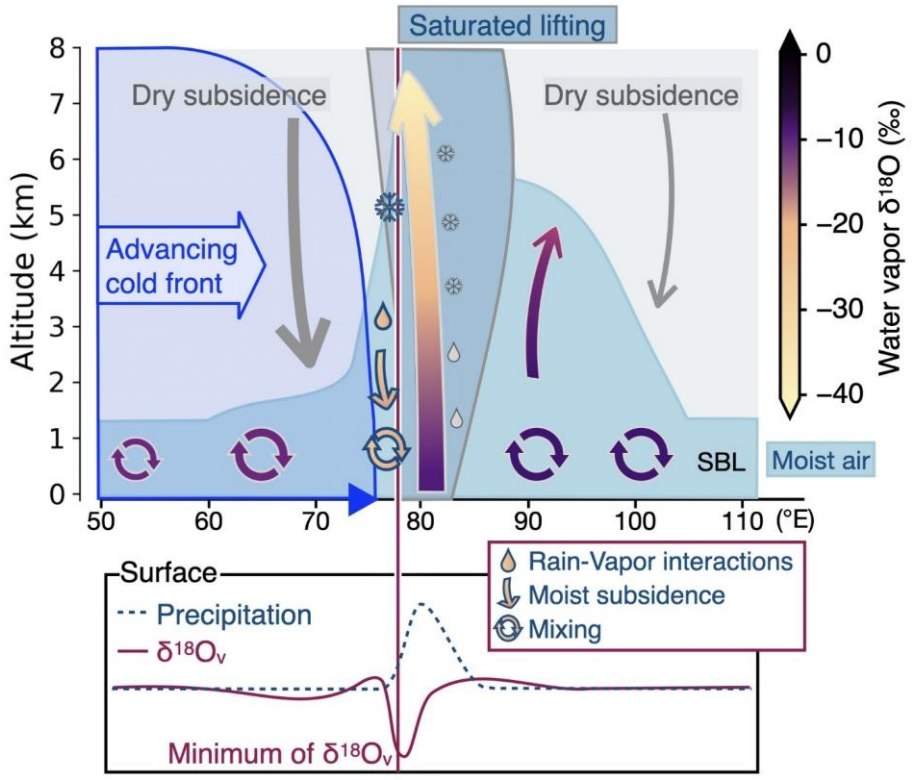

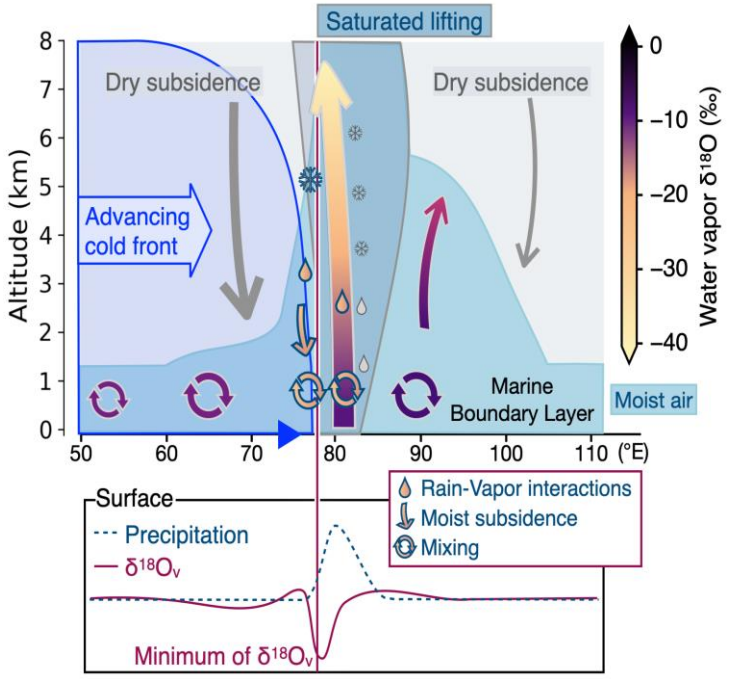

Figure ~~8~~9: Scheme of the mechanism explaining the sharp negative excursion of $\delta^{18}O_v$ recorded at the surface for cold front events associated with precipitation. The scheme is based on the profile modelled by ECHAM6-wiso for event of January 9th 2020 (see supplementary material Figure S5). The top panel show the altitude vs longitude dynamics of air masses with vertical saturated lifting in the center and subsidence at the rear of the lifting. The bottom panel shows the associated evolution of $\delta^{18}O_v$ and precipitations on the same longitude scale than on the upper panel.

Mis en forme: Exposant

5. Conclusion

We presented here the first water vapor isotopic record over 2 years ~~in~~ on Amsterdam Island. The water vapor isotopic variations follow at first order the variations of water vapor mixing ratio as expected for such a~~from a~~ marine site. Superimposed to this variability, we have evidenced 11 periods of a few hours characterized by the occurrence of one or two abrupt negative excursions of $\delta^{18}O_v$ ~~/ days where~~ while the correlation between $\delta^{18}O_v$ and water vapor mixing ratio does not hold. ~~These periods are associated with the occurrence of one or two~~

~~abrupt negative excursions of $\delta^{18}O_v$.~~ These negative excursions ~~associated with cold fronts~~ are often occurring toward the end of precipitation events. They are most of the time characterized by a decrease in water vapor mixing ratio. Representation of these short events is a challenge for the atmospheric components of Earth System Models equipped with water isotopes and we found that the ECHAM6-wiso model was able to reproduce most of the sharp negative $\delta^{18}O_v$ excursions while the LMDZ-iso model at ~~2°~~low (very low~~3°~~) resolution was only able to reproduce 7 (1) of the negative excursions. The good agreement between modeled and measured $\delta^{18}O_v$ when using ECHAM6-wiso validates the physics processes within the ECHAM6-wiso model as well as the implemented physics of water isotopes.

Using previous modeling studies as well as information provided by (1) the confrontation with other data sources (GEM, meteorology) obtained in parallel on this site, (2) back trajectory analyses and (3) the outputs of the two models ECHAM6-wiso and LMDZ-iso, we conclude that the most plausible explanations for such events are rain-vapor interactions and subsidence at the rear of a precipitation event. Both can be combined, since rain vapor interactions can help maintaining moist conditions in subsidence regions.

This study highlight~~ed~~s the added value of combining different data from an atmospheric observatory to understand the dynamics of the atmospheric circulation. These ~~two~~2-year records are also a good benchmark for model evaluation. We have especially shown that the isotopic composition of water vapor measured at the surface is a powerful tool to identify aspects to be improved in the atmospheric component of the ~~general circulation~~Earth system models. In our case, we used it to test different~~, such as the~~ horizontal resolutions which ~~may~~ influence the representativity of the vertical dynamics and have important implication in the simulation of surface variations of water vapor $\delta^{18}O_v$. Our study highlights the importance to have high-resolution models (e.g. mesoscale models) equipped with isotopes to further study such abrupt isotopic events.

Mis en forme: Couleur de police : Automatique

Mis en forme: Police :Symbol

Mis en forme: Exposant

Mis en forme: Indice

Appendices:

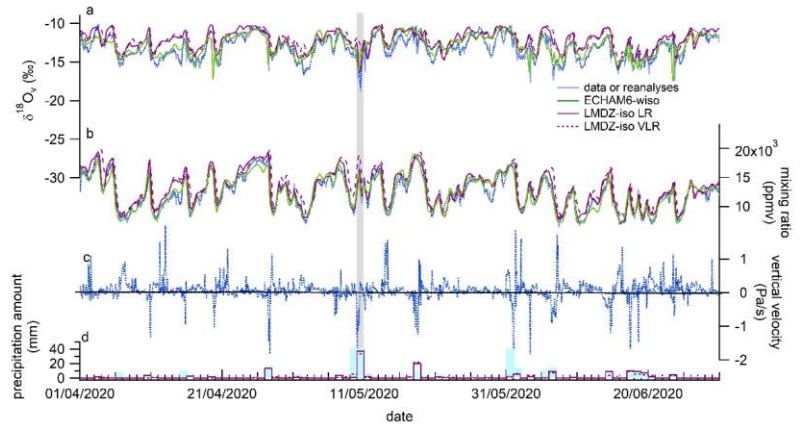

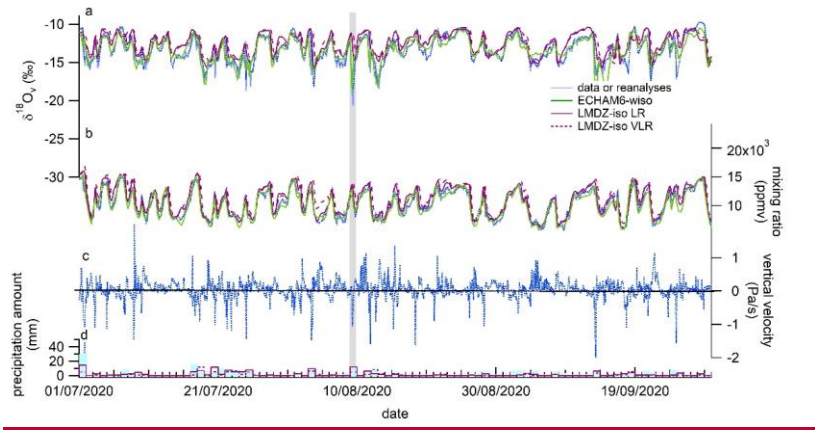

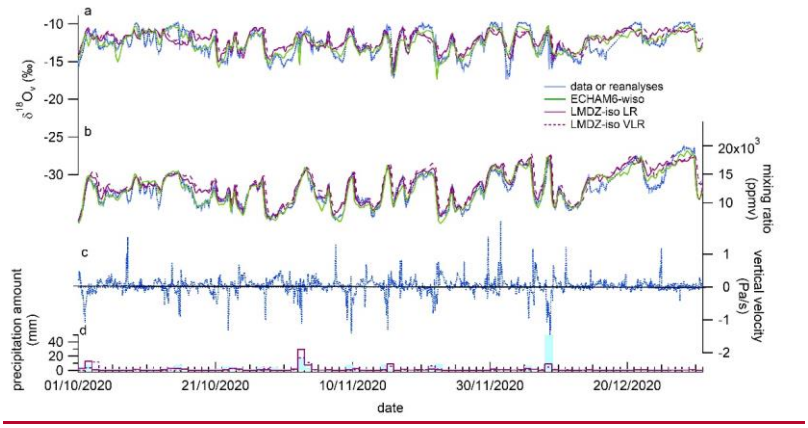

Mis en forme: Police :14 pt, Gras

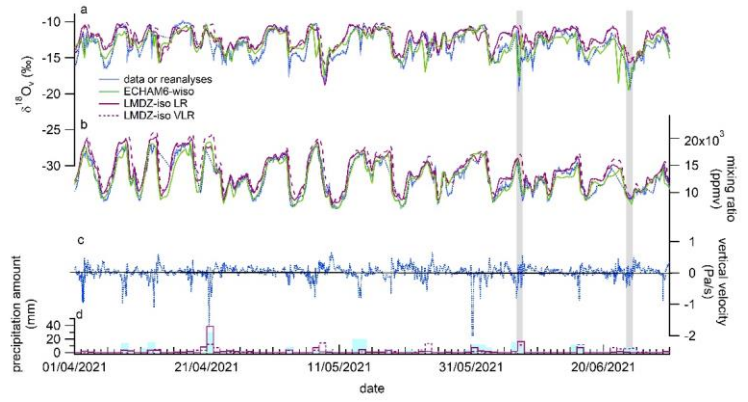
a
b
c
d
data or reanalyses
ECHAM6-wiso
LMDZ-iso LR
LMDZ-iso VLR
δ18Ov (‰)
mixing ratio (ppmv)
vertical velocity (Pa/s)
precipitation amount (mm)
01/04/2021
21/04/2021
11/05/2021
31/05/2021
20/06/2021
date

306

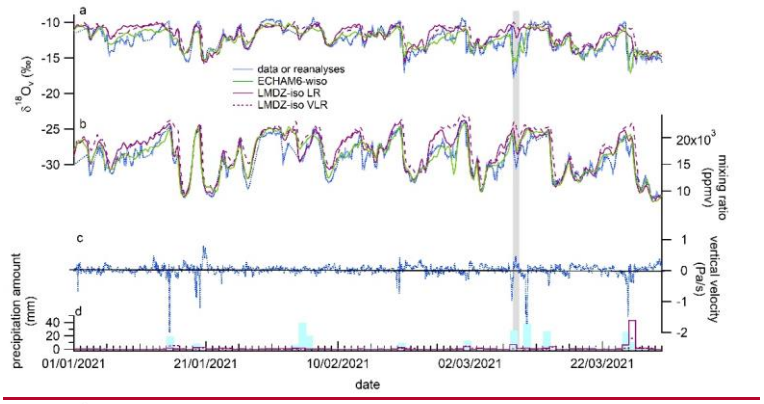
a
b
c
d
data or reanalyses
ECHAM6-wiso
LMDZ-iso LR
LMDZ-iso VLR
δ18Ov (‰)
mixing ratio (ppmv)
vertical velocity (Pa/s)
precipitation amount (mm)
01/01/2021
21/01/2021
10/02/2021
02/03/2021
22/03/2021
date

307

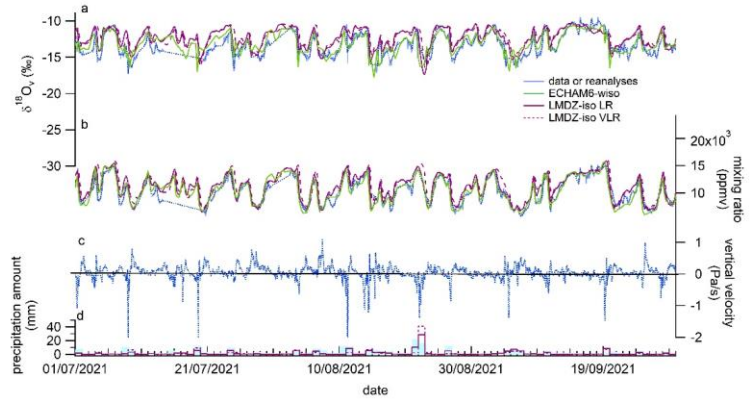
a
b
c
d
data or reanalyses
ECHAM6-wiso
LMDZ-iso LR
LMDZ-iso VLR
δ18Ov (‰)
mixing ratio (ppmv)
vertical velocity (Pa/s)
precipitation amount (mm)
01/07/2021
21/07/2021
10/08/2021
30/08/2021
19/09/2021
date

308

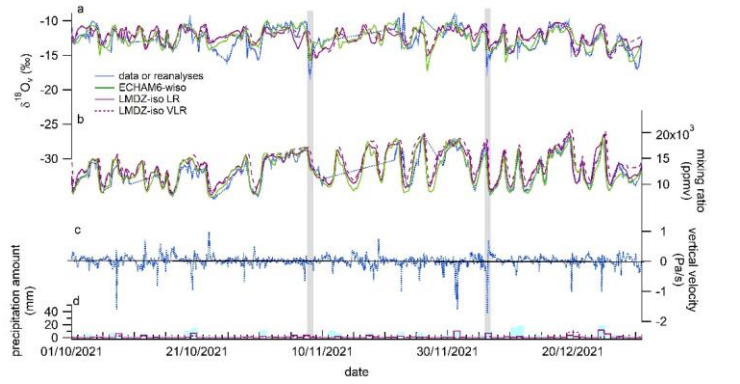

Figure A1: Model-measurement comparison (April 2020 – December 2021): a- $\delta^{18}O_v$ (light blue for data on hourly average, dark blue for data resampled at a 6-hour resolution); b- water vapor mixing ratio from our data set; c- vertical velocity; d- Precipitation amount. The grey shadings highlight the negative $\delta^{18}O_v$ excursions.

Mis en forme: Police :14 pt, Gras
Mis en forme: Police :Gras
Mis en forme: Police :Gras, Soulignement
Mis en forme: Police :(Par défaut) Times New Roman
Mis en forme: Police :(Par défaut) Times New Roman
Mis en forme: Police :(Par défaut) Times New Roman
Mis en forme: Police :(Par défaut) Times New Roman
Mis en forme: Police :Symbol
Mis en forme: Police :(Par défaut) Times New Roman
Mis en forme: Police :(Par défaut) Times New Roman
Mis en forme: Police :(Par défaut) Times New Roman
Mis en forme: Police :(Par défaut) Times New Roman

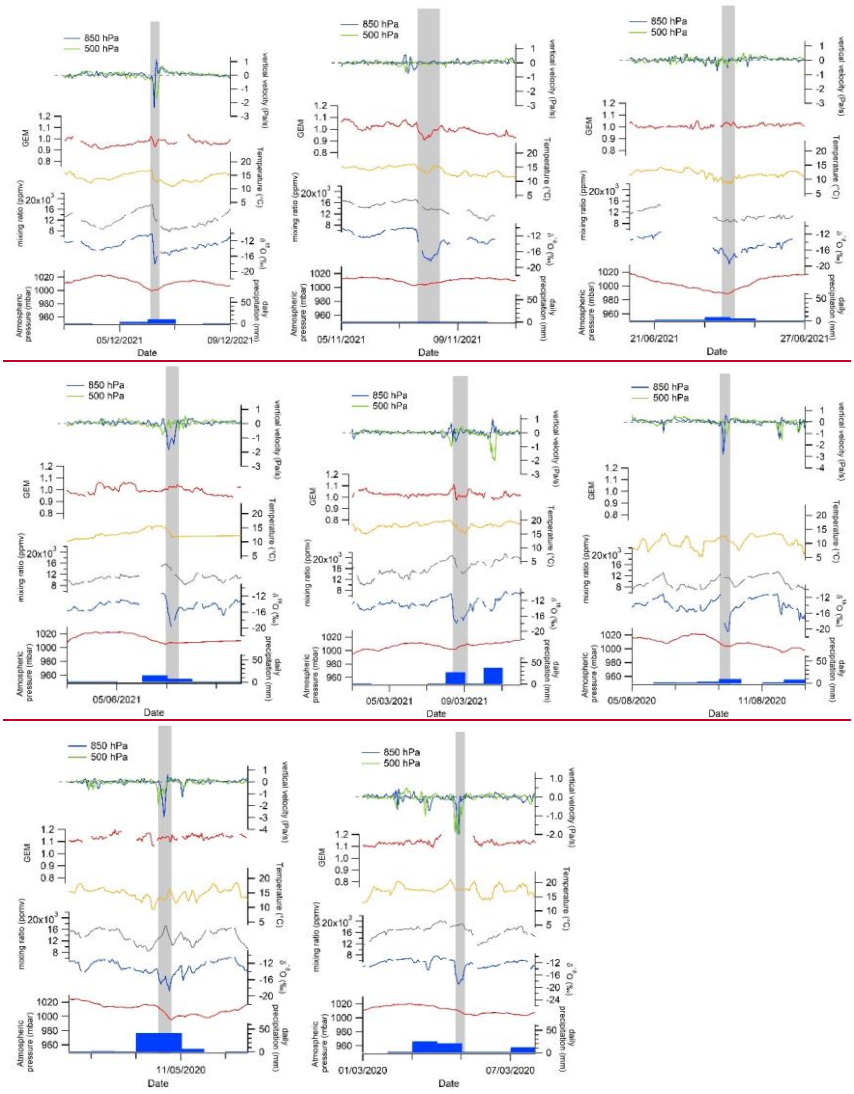

Figure A2 : Evolution of GEM, $\delta^{18}O_v$, water vapor mixing ratio, meteorological parameters (surface temperature, surface atmospheric pressure, daily precipitation) measured by the MeteoFrance weather station and vertical velocity from the ERA5 reanalyses at 500 and 850 hPa over the isotopic excursions between March 2020 and December 2021.

Mis en forme: Police :(Par défaut) Times New Roman, 12 pt

Mis en forme: Police :(Par défaut) Times New Roman, 12 pt

Mis en forme: Interligne : 1.5 ligne

Mis en forme: Police :Symbol

Mis en forme: Police :(Par défaut) Times New Roman, 12 pt

Mis en forme: Contour du texte

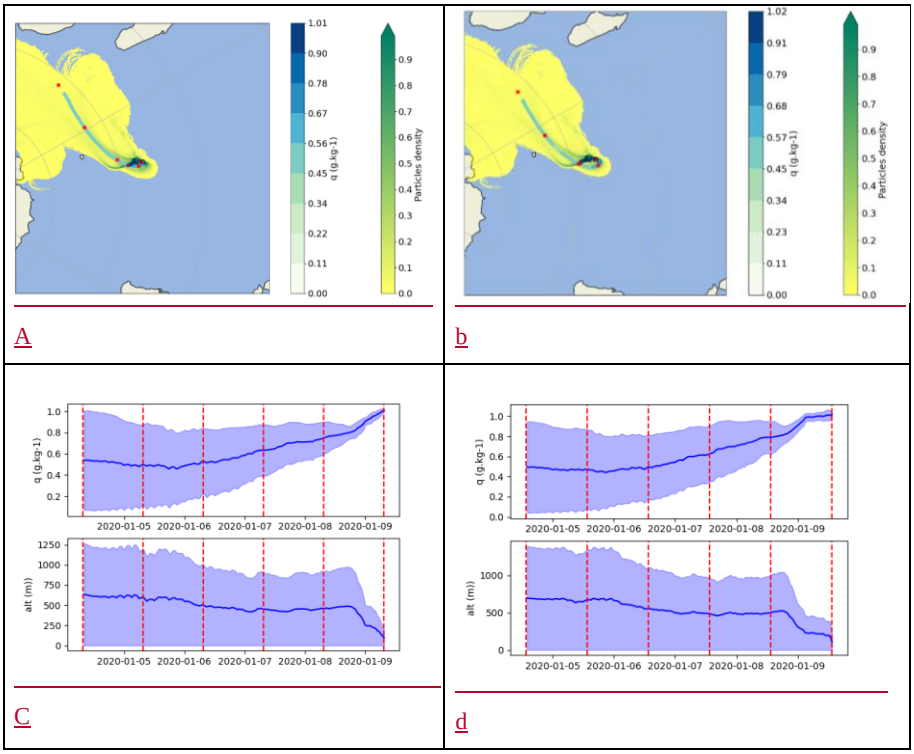

Figure A3: FLEXPART footprints of 5-day back trajectories for the event of January 9th 2020. (a) Latitude-longitude projection of the FLEXPART back trajectory footprint for January 9th 2020 at 7h30. The yellow to green colors on each grid point of these projections represent the density of particles. The white to blue colors indicate the water vapor mixing ratio on the humidity weighted average back-trajectory. Each red point indicates the location of the average back-trajectory for each of the 5 days before the date of the considered event. (b) Same as a for January 9th 2020 at 13h30. (c) Top shows the evolution of the water vapor mixing ratio of the back trajectories for January 9th 2020 at 7h30; bottom shows the altitude evolution of the back trajectory for January 9th 2020 at 7h30. (d) same as (c) for January 9th 2020 at 13h30.

Mis en forme: Police :Gras, Couleur de police : Automatique

Mis en forme: Couleur de police : Automatique

Mis en forme: Couleur de police : Automatique, Exposant

Mis en forme: Couleur de police : Automatique

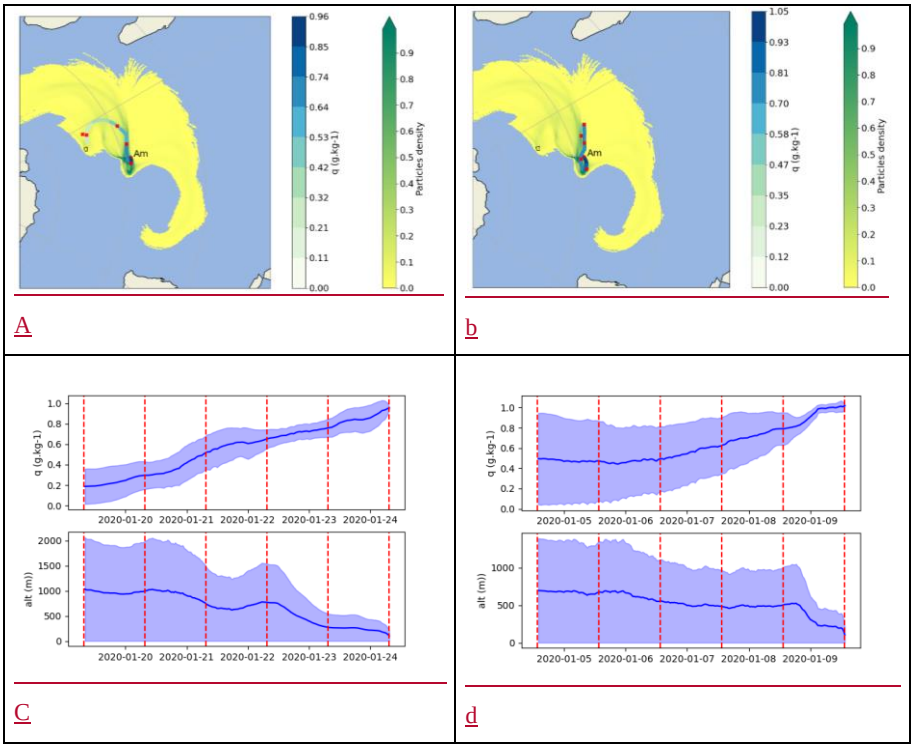

Figure A4: FLEXPART footprints of 5-day back trajectories for the event of January 21st 2020. (a) Latitude-longitude projection of the FLEXPART back trajectory footprint for January 21st 2020 at 7h30. The yellow to green colors on each grid point of these projections represent the density of particles. The white to blue colors indicate the water vapor mixing ratio on the humidity weighted average back-trajectory. Each red point indicates the location of the average back-trajectory for each of the 5 days before the date of the considered event. (b) Same as a for January 21st 2020 at 13h00. (c) Top shows the evolution of the water vapor mixing ratio of the back trajectories for January 21st 2020 at 7h30; bottom shows the altitude evolution of the back trajectory for January 21st 2020 at 7h30. (d) same as (c) for January 21st 2020 at 13h00.

Mis en forme: Couleur de police : Automatique

Data availability: AMS L2 GEM data (https://doi.org/10.25326/168) are freely available (Magand and Dommergue, 2021~~+~~2) at https://gmos.aeris-data.fr/ from national GMOS-FR

website data portal coordinated by IGE (Institut des Géosciences de l'Environnement, Grenoble, France; technical PI: Olivier Magand) with the support of the French national AERIS-SEDOO partners, data and services center for the atmosphere (last access: 08 December 2022). Hg species measurements belong to international monitoring networks (http://www.gos4m.org/). Water isotopic data and modeling outputs are available on the Zenodo platform (https://zenodo.org/record/8164392; https://zenodo.org/record/8160871).

Acknowledgements: We deeply thank all overwintering staff at AMS and the French Polar Institute Paul-Emile Victor (IPEV) staff and scientists who helped with the setup and maintenance of the experiment at AMS in the framework of the GMOStral-1028 IPEV program, the ICOS-416 program and the ADELISE-1205 IPEV program. Amsterdam Island Hg0 data, accessible in national GMOS-FR website data portal ~~(https://gmos.aeris-data.fr/)~~ were collected via instruments coordinated by the IGE-PTICHA technical platform dedicated to atmospheric chemistry field instrumentation. GMOS-FR data portal is maintained by the French national center for Atmospheric data and services AERIS, which is acknowledged by the authors. The LMDZ-iso simulation were performed thanks to granted access to the HPC resources of IDRIS under the allocations 2022-AD010114000 and 2022-AD010107632R1 and made by GENCI. We deeply thank Sébastien Nguyen (CEA, LSCE) for his help and support in running LMDZiso simulation.

Funding: This work benefited from the IPSL-CGS EUR and was supported by a grant from the French government under the Programme d'Investissements d'avenir, reference ANR-11-IDEX-0004-17-EURE-0006, managed by the Agence Nationale de la Recherche. This project has also been supported by the LEFE IMAGO project ADELISE. Amsterdam Island GEM data, accessible in national GMOS-FR website data portal ~~(https://gmos.aeris-data.fr/)~~ have been collected with funding from European Union 7th Framework Programme project Global Mercury Observation System (GMOS 2010-2015 Nr. 26511), the French Polar Institute IPEV via GMOStral-1028 IPEV program since 2012, the LEFE CHAT CNRS/INSU (TOPMMODEL project, Nr. AO2017-984931) and the H2020 ERA-PLANET (Nr. 689443) iGOSP program. This work is part of the AWACA project that has received funding from the European Research Council (ERC) under the European Union's Horizon 2020 research and innovation programme (Grant agreement No. 951596). The ERA5 reanalyses files for the ECHAM6-wiso nudging have been provided by the German Climate Computing Center

Mis en forme: Couleur de soulignement : Couleur personnalisée(RVB(0;0;10)),Couleur de police : Couleur personnalisée(RVB(0;0;10))

(DKRZ). The ECHAM6-wiso simulations have been performed with support of the Alfred Wegener Institute (AWI) supercomputing centre.

Author contributions: AL designed the study and analyzed the data together with FV, CS, EF, OM. OC installed the water vapor isotopic analyzer in Amsterdam Island and OJ was in charge of the data calibration. BM and FP performed the measurements of the isotopic composition of the precipitation samples. CA analyzed the modeling outputs, realized most of the simulations and performed model-data analyses. CLDS performed the back trajectory analyses with help from MC. OM, AD and YB provided expertise on GEM analyses and interpretation. AC, CR, ND and MW provided model simulations. AL wrote the paper with contribution of all coauthors.

Competing interests: One of the coauthors (AD) is a member of the editorial board of Atmospheric Chemistry and Physics.

References

Aemisegger, F., Sturm, P., Graf, P., Sodemann, H., Pfahl, S., Knohl, A., and Wernli, H.: Measuring variations of d18O and d2H in atmospheric water vapour using two commercial laser-based spectrometers: an instrument characterisation study, Atmospheric Measurement Techniques, 5, 1491–1511, https://doi.org/10.5194/amt-5-1491-2012, 2012.

Aemisegger, F., Spiegel, J., Pfahl, S., Sodemann, H., Eugster, W., and Wernli, H.: Isotope meteorology of cold front passages: A case study combining observations and modeling, Geophysical Research Letters, 42, 5652–5660, 2015.

Angot, H., Barret, M., Magand, O., Ramonet, M., and Dommergue, A.: A 2-year record of atmospheric mercury species at a background Southern Hemisphere station on Amsterdam Island, Atmospheric Chemistry and Physics, 14, 11461–11473, 2014.

Angot, H., Dion, I., Vogel, N., Legrand, M., Magand, O., and Dommergue, A.: Multi-year record of atmospheric mercury at Dumont d'Urville, East Antarctic coast: continental outflow and oceanic influences, Atmospheric Chemistry and Physics, 16, 8265–8279, 2016.

Ansari, M. A., Noble, J., Deodhar, A., and Kumar, U. S.: Atmospheric factors controlling the stable isotopes (δ18O and δ2H) of the Indian summer monsoon precipitation in a drying region of Eastern India, Journal of Hydrology, 584, 124636, 2020.

Arias, P., Bellouin, N., Coppola, E., Jones, R., Krinner, G., Marotzke, J., Naik, V., Palmer, M., Plattner, G.-K., Rogelj, J., and others: Climate Change 2021: the physical science basis. Contribution of Working Group I to the Sixth Assessment Report of the Intergovernmental Panel on Climate Change; technical summary, 2021.

Bailey, A., Aemisegger, F., Villiger, L., Los, S. A., Reverdin, G., Quiñones Meléndez, E., Acquistapace, C., Baranowski, D. B., Böck, T., Bony, S., Bordsdorff, T., Coffman, D., de Szoeke, S. P., Diekmann, C. J., Dütsch, M., Ertl, B., Galewsky, J., Henze, D., Makuch, P., Noone, D., Quinn, P. K., Rösch, M., Schneider, A., Schneider, M., Speich, S., Stevens, B., and Thompson, E. J.: Isotopic measurements in water vapor, precipitation, and seawater during EUREC^{4}A, Earth System Science Data, 15, 465–495, https://doi.org/10.5194/essd-15-465-2023, 2023.

Benetti, M., Reverdin, G., Pierre, C., Merlivat, L., Risi, C., Steen-larsen, H. C., and Vimeux, F.: Journal of Geophysical Research : Atmospheres during evaporation, 584–593, https://doi.org/10.1002/2013JD020535.Received, 2014.

Benetti, M., Aloisi, G., Reverdin, G., Risi, C., and Sèze, G.: Importance of boundary layer mixing for the isotopic composition of surface vapor over the subtropical North Atlantic Ocean, Journal of Geophysical Research: Atmospheres, 120, 2190–2209, 2015.

Bhattacharya, S. K., Sarkar, A., and Liang, M.-C.: Vapor isotope probing of typhoons invading the Taiwan region in 2016, Journal of Geophysical Research: Atmospheres, 127, e2022JD036578, 2022.

Bloom, N. and Fitzgerald, W. F.: Determination of volatile mercury species at the picogram level by low-temperature gas chromatography with cold-vapour atomic fluorescence detection, Analytica Chimica Acta, 208, 151–161, 1988.

Bonne, J. L., Behrens, M., Meyer, H., Kipfstuhl, S., Rabe, B., Schönicke, L., Steen-Larsen, H. C., and Werner, M.: Resolving the controls of water vapour isotopes in the Atlantic sector, Nature Communications, 10, 1–10, https://doi.org/10.1038/s41467-019-09242-6, 2019.

Boucher, O., Servonnat, J., Albright, A. L., Aumont, O., Balkanski, Y., Bastrikov, V., Bekki, S., Bonnet, R., Bony, S., Bopp, L., Braconnot, P., Brockmann, P., Cadule, P., Caubel, A., Cheruy, F.,

946 Codron, F., Cozic, A., Cugnet, D., D'Andrea, F., Davini, P., de Lavergne, C., Denvil, S., Deshayes, J.,
947 Devilliers, M., Ducharne, A., Dufresne, J.-L., Dupont, E., Éthé, C., Fairhead, L., Falletti, L., Flavoni,
948 S., Foujols, M.-A., Gardoll, S., Gastineau, G., Ghattas, J., Grandpeix, J.-Y., Guenet, B., Guez, E.,
949 Lionel, Guilyardi, E., Guimberteau, M., Hauglustaine, D., Hourdin, F., Idelkadi, A., Joussaume, S.,
950 Kageyama, M., Khodri, M., Krinner, G., Lebas, N., Levavasseur, G., Lévy, C., Li, L., Lott, F., Lurton,
951 T., Luyssaert, S., Madec, G., Madeleine, J.-B., Maignan, F., Marchand, M., Marti, O., Mellul, L.,
952 Meurdesoif, Y., Mignot, J., Musat, I., Ottlé, C., Peylin, P., Planton, Y., Polcher, J., Rio, C., Rochetin,
953 N., Rousset, C., Sepulchre, P., Sima, A., Swingedouw, D., Thiéblemont, R., Traore, A. K.,
954 Vancoppenolle, M., Vial, J., Vialard, J., Viovy, N., and Vuichard, N.: Presentation and Evaluation of
955 the IPSL-CM6A-LR Climate Model, Journal of Advances in Modeling Earth Systems, 12,
956 e2019MS002010, https://doi.org/10.1029/2019MS002010, 2020.

957 Bréant, C., Leroy Dos Santos, C., Agosta, C., Casado, M., Fourré, E., Goursaud, S., Masson-Delmotte,
958 V., Favier, V., Cattani, O., Prié, F., Golly, B., Orsi, A., Martinerie, P., and Landais, A.: Coastal water
959 vapor isotopic composition driven by katabatic wind variability in summer at Dumont d'Urville,
960 coastal East Antarctica, Earth and Planetary Science Letters, 514, 37–47,
961 https://doi.org/10.1016/j.epsl.2019.03.004, 2019.

962 Brooks, S.; Ren, X. R.; Cohen, M.; Luke, W. T.; Kelley, P.; Artz, R.; Hynes, A.; Landing, W.; Martos,
963 B. Airborne vertical profiling of mercury speciation near Tullahoma, TN,
964 USA Atmosphere 2014, 5 (3) 557– 574 DOI: 10.3390/atmos5030557.
965
966 Casado, M., Landais, A., Masson-Delmotte, V., Genthon, C., Kerstel, E., Kassi, S., Arnaud, L., Picard,
967 G., Prie, F., Cattani, O., Steen-Larsen, H.-C., Vignon, E., and Cermak, P.: Continuous measurements
968 of isotopic composition of water vapour on the East Antarctic Plateau, Atmospheric Chemistry and
969 Physics, 16, https://doi.org/10.5194/acp-16-8521-2016, 2016.

970 Cauquoin, A. and Werner, M.: High-Resolution Nudged Isotope Modeling With ECHAM6-Wiso:
971 Impacts of Updated Model Physics and ERA5 Reanalysis Data, Journal of Advances in Modeling
972 Earth Systems, 13, e2021MS002532, https://doi.org/10.1029/2021MS002532, 2021.

973 Cauquoin, A., Werner, M., and Lohmann, G.: Water isotopes -- climate relationships for the mid-
974 Holocene and preindustrial period simulated with an isotope-enabled version of MPI-ESM, Climate of
975 the Past, 15, 1913–1937, https://doi.org/10.5194/cp-15-1913-2019, 2019.

976 Craig, H.: Isotopic Variations in Meteoric Waters, Science, 133, 1702–1703,
977 https://doi.org/10.1126/science.133.3465.1702, 1961.

978 Dahinden, F., Aemisegger, F., Wernli, H., Schneider, M., Diekmann, C. J., Ertl, B., Knippertz, P.,
979 Werner, M., and Pfahl, S.: Disentangling different moisture transport pathways over the eastern
980 subtropical North Atlantic using multi-platform isotope observations and high-resolution numerical
981 modelling, Atmospheric Chemistry and Physics, 21, 16319–16347, https://doi.org/10.5194/acp-21-
982 16319-2021, 2021.

983 Dansgaard, W.: Stable isotopes in precipitation., Tellus, 16, 436–468, 1964.

984 Dumarey, R., Temmerman, E., Adams, R., and Hoste, J.: The accuracy of the vapour-injection
985 calibration method for the determination of mercury by amalgamation/cold-vapour atomic absorption
986 spectrometry, Analytica Chimica Acta, 170, 337–340, 1985.

987 Durack, P. J., Taylor, K. E., Ames, S., Po-Chedley, S., and Mauzey, C.: PCMDI AMIP SST and sea-
988 ice boundary conditions version 1.1.8, , https://doi.org/10.22033/ESGF/input4MIPs.16921, 2022.

989 Dütsch, M., Pfahl, S., and Wernli, H.: Drivers of δ2H variations in an idealized extratropical cyclone,
990 Geophysical Research Letters, 43, 5401–5408, 2016.

Edwards, B. A., Kushner, D. S., Outridge, P. M., Wang, F. (2021). Fifty years of volcanic mercury emission research: Knowledge gaps and future directions. *Science of The Total Environment*, *757*, 143800. https://doi.org/10.1016/j.scitotenv.2020.143800.

El Yazidi, A., Ramonet, M., Ciais, P., Broquet, G., Pison, I., Abbaris, A., Brunner, D., Conil, S., Delmotte, M., Gheusi, F., and others: Identification of spikes associated with local sources in continuous time series of atmospheric CO, CO_2 and CH_4, Atmospheric Measurement Techniques, 11, 1599–1614, 2018.

Eyring, V., Bony, S., Meehl, G. A., Senior, C. A., Stevens, B., Stouffer, R. J., and Taylor, K. E.: Overview of the Coupled Model Intercomparison Project Phase 6 (CMIP6) experimental design and organization, Geoscientific Model Development, 9, 1937–1958, https://doi.org/10.5194/gmd-9-1937-2016, 2016.

Fain, X.; Obrist, D.; Hallar, A. G.; Mccubbin, I.; Rahn, T. High levels of reactive gaseous mercury observed at a high elevation research laboratory in the Rocky Mountains Atmos. Chem. Phys. 2009, 9 (20) 8049– 8060 DOI: 10.5194/acp-9-8049-2009.

Fitzgerald, W. F. and Gill, G. A.: Subnanogram determination of mercury by two-stage gold amalgamation and gas phase detection applied to atmospheric analysis, Analytical chemistry, 51, 1714–1720, 1979.

Fogt, R. and Marshall, G.: The Southern Annular Mode: Variability, trends, and climate impacts across the Southern Hemisphere, Wiley Interdisciplinary Reviews: Climate Change, 11, https://doi.org/10.1002/wcc.652, 2020.

Fu, X., Marusczak, N., Wang, X., Gheusi, F. and Sonke, J.: The isotopic composition of gaseous elemental mercury in the free troposphere of the Pic du Midi Observatory, France. Environmental Science & Technology. 50. 10.1021/acs.est.6b00033, 2016

Galewsky, J., Steen-Larsen, H. C., Field, R. D., Worden, J., Risi, C., and Schneider, M.: Stable isotopes in atmospheric water vapor and applications to the hydrologic cycle, Reviews of Geophysics, 54, 809–865, 2016.

Gaudry, A., Ascencio, J., and Lambert, G.: Preliminary study of CO2 variations at Amsterdam Island (Territoire des Terres Australes et Antarctiques Francaises), Journal of Geophysical Research: Oceans, 88, 1323–1329, 1983.

Graf, P., Wernli, H., Pfahl, S., and Sodemann, H.: A new interpretative framework for below-cloud effects on stable water isotopes in vapour and rain, Atmospheric Chemistry and Physics, 19, 747–765, 2019.

Gros, V., Poisson, N., Martin, D., Kanakidou, M., and Bonsang, B.: Observations and modeling of the seasonal variation of surface ozone at Amsterdam Island: 1994–1996, Journal of Geophysical Research: Atmospheres, 103, 28103–28109, 1998.

Gros, V., Bonsang, B., Martin, D., Novelli, P., and Kazan, V.: Carbon monoxide short term measurements at Amsterdam island: estimations of biomass burning emission rates, Chemosphere-Global Change Science, 1, 163–172, 1999.

Gaffney J, Marley N. In-depth review of atmospheric mercury: sources, transformations, and potential sinks. *Energy and Emission Control Technologies*. 2014;2:1-21https://doi.org/10.2147/EECT.S37038.

Guilpart, E., Vimeux, F., Evan, S., Brioude, J., Metzger, J., Barthe, C., Risi, C., and Cattani, O.: The isotopic composition of near-surface water vapor at the Maïdo observatory (Reunion Island,

southwestern Indian Ocean) documents the controls of the humidity of the subtropical troposphere, Journal of Geophysical Research: Atmospheres, 122, 9628–9650, https://doi.org/10.1002/2017JD026791, 2017.

Gustin, M. S., Amos, H. M., Huang, J., Miller, M. B., and Heidecorn, K.: Measuring and modeling mercury in the atmosphere: a critical review, Atmos. Chem. Phys., 15, 5697–5713, https://doi.org/10.5194/acp-15-5697-2015, 2015.

Gustin, M. S., Bank, M. S., Bishop, K., Bowman, K., Brafireun, B., Chételat, J., Eckley, C. S., Hammerschmidt, C. R., Lamborg, C., Lyman, S., Martínez-Cortizas, A., Sommar, J., Tsz-Ki Tsui, M., & Zhang, T. (2020). Mercury biogeochemical cycling: A synthesis of recent scientific advances. Science of the Total Environment, 737, 139619. https://doi.org/10.1016/j.scitotenv.2020.139619.

Gworek, B., Dmuchowski, W. & Baczewska-Dąbrowska, A.H. Mercury in the terrestrial environment: a review. Environ Sci Eur **32**, 128 (2020). https://doi.org/10.1186/s12302-020-00401-x.

Henze, D., Noone, D., and Toohey, D.: Aircraft measurements of water vapor heavy isotope ratios in the marine boundary layer and lower troposphere during ORACLES, Earth Syst. Sci. Data, 14, 1811–1829, https://doi.org/10.5194/essd-14-1811-2022, 2022.

Hersbach, H., Bell, B., Berrisford, P., Hirahara, S., Horányi, A., Muñoz-Sabater, J., Nicolas, J., Peubey, C., Radu, R., Schepers, D., Simmons, A., Soci, C., Abdalla, S., Abellan, X., Balsamo, G., Bechtold, P., Biavati, G., Bidlot, J., Bonavita, M., De Chiara, G., Dahlgren, P., Dee, D., Diamantakis, M., Dragani, R., Flemming, J., Forbes, R., Fuentes, M., Geer, A., Haimberger, L., Healy, S., Hogan, R. J., Hólm, E., Janisková, M., Keeley, S., Laloyaux, P., Lopez, P., Lupu, C., Radnoti, G., de Rosnay, P., Rozum, I., Vamborg, F., Villaume, S., and Thépaut, J.-N.: The ERA5 global reanalysis, Quarterly Journal of the Royal Meteorological Society, 146, 1999–2049, https://doi.org/10.1002/qj.3803, 2020.

Hoang, C., Magand, O., Brioude, J., Dimuro, A., Brunet, C., Ah-Peng, C., Bertrand, Y., Dommergue, A., Lei, Y. D., and Wania, F.: Probing the limits of sampling gaseous elemental mercury passively in the remote atmosphere, Environ. Sci.: Atmos., 3, 268–281, https://doi.org/10.1039/D2EA00119E, 2023.

Hourdin, F., Rio, C., Grandpeix, J.-Y., Madeleine, J.-B., Cheruy, F., Rochetin, N., Jam, A., Musat, I., Idelkadi, A., Fairhead, L., Foujols, M.-A., Mellul, L., Traore, A.-K., Dufresne, J.-L., Boucher, O., Lefebvre, M.-P., Millour, E., Vignon, E., Jouhaud, J., Diallo, F. B., Lott, F., Gastineau, G., Caubel, A., Meurdesoif, Y., and Ghattas, J.: LMDZ6A: The Atmospheric Component of the IPSL Climate Model With Improved and Better Tuned Physics, Journal of Advances in Modeling Earth Systems, 12, e2019MS001892, https://doi.org/10.1029/2019MS001892, 2020.

Jiskra, M., Sonke, J. E., Obrist, D., Bieser, J., Ebinghaus, R., Myhre, C. L., Pfaffhuber, K. A., Wängberg, I., Kyllönen, K., Worthy, D., Martin, L. G., Labuschagne, C., Mkololo, T., Ramonet, M., Magand, O., and Dommergue, A.: A vegetation control on seasonal variations in global atmospheric mercury concentrations, Nature Geoscience, 11, 244–250, https://doi.org/10.1038/s41561-018-0078-8, 2018.

Jullien, N., Vignon, É., Sprenger, M., Aemisegger, F., and Berne, A.: Synoptic conditions and atmospheric moisture pathways associated with virga and precipitation over coastal Adélie Land in Antarctica, The Cryosphere, 14, 1685–1702, https://doi.org/10.5194/tc-14-1685-2020, 2020.

Koening, A.M., Magand, O., Verreyken, B., Brioude, J., Amelynck, C., Schoon, N., Colomb, A., Ramonet, M., Sha, M.K., Cammas, J.P., Sonke, J.E., Dommergue, A., 2023. Mercury in the free troposphere and bidirectional atmosphere-vegetation exchanges – Insights from Maido observatory in

Mis en forme: Police :(Par défaut) Times New Roman, 11 pt

Mis en forme: Police par défaut, Couleur de police : Noir

Mis en forme: Corps

1086 the southern hemisphere tropics. Atmos. Chem. Phys., 23, 1309-1328, https://doi.org/10.5194/acp-23-
1087 1309-2023
1088
1089 Lee, K.-O., Aemisegger, F., Pfahl, S., Flamant, C., Lacour, J.-L., and Chaboureau, J.-P.: Contrasting
1090 stable water isotope signals from convective and large-scale precipitation phases of a heavy
1091 precipitation event in southern Italy during HyMeX IOP 13: a modelling perspective, Atmospheric
1092 Chemistry and Physics, 19, 7487–7506, 2019.

1093 LeGrande, A. N. and Schmidt, G. A.: Global gridded data set of the oxygen isotopic composition in
1094 seawater, Geophysical Research Letters, 33, 1–5, https://doi.org/10.1029/2006GL026011, 2006.

1095 Leroy-Dos Santos, C., Masson-Delmotte, V., Casado, M., Fourré, E., Steen-Larsen, H. C., Maturilli,
1096 M., Orsi, A., Berchet, A., Cattani, O., Minster, B., Gherardi, J., and Landais, A.: A 4.5 Year-Long
1097 Record of Svalbard Water Vapor Isotopic Composition Documents Winter Air Mass Origin, Journal
1098 of Geophysical Research: Atmospheres, 125, e2020JD032681-e2020JD032681,
1099 https://doi.org/10.1029/2020JD032681, 2020.

1100 Leroy-Dos Santos, C., Casado, M., Prié, F., Jossoud, O., Kerstel, E., Farradèche, M., Kassi, S., Fourré,
1101 E., and Landais, A.: A dedicated robust instrument for water vapor generation at low humidity for use
1102 with a laser water isotope analyzer in cold and dry polar regions, Atmospheric Measurement
1103 Techniques, 14, 2907–2918, https://doi.org/10.5194/amt-14-2907-2021, 2021.

1104 Li, C., Enrico, M., Magand, O., Araujo, B. F., Le Roux, G., Osterwalder, S., Dommergue, A.,
1105 Bertrand, Y., Brioude, J., De Vleeschouwer, F., and others: A peat core Hg stable isotope
1106 reconstruction of Holocene atmospheric Hg deposition at Amsterdam Island (37.8 oS), Geochimica et
1107 Cosmochimica Acta, 341, 62–74, 2023.

1108 Lindberg, S., Bullock, R., Ebinghaus, R., Engstrom, D., Feng, X., Fitzgerald, W., Pirrone, N., Prestbo,
1109 E., and Seigneur, C.: A synthesis of progress and uncertainties in attributing the sources of mercury in
1110 deposition., Ambio, 36, 19–32, 2007, https://doi.org/10.1579/0044-7447(2007)

1111 Lyman, S. N.; Jaffe, D. A. Formation and fate of oxidized mercury in the upper troposphere and lower
1112 stratosphere Nat. Geosci. 2012, 5 (2) 114– 117 doi: 10.1038/ngeo1353
1113
1114 Magand, O. and Dommergue, A.: Continuous measurements of atmospheric mercury at Maido
1115 Observatory (L2), Global Mercury Observation System [data set], 2022.

1116 Munksgaard, N. C., Zwart, C., Kurita, N., Bass, A., Nott, J., and Bird, M. I.: Stable isotope anatomy of
1117 tropical cyclone Ita, north-eastern Australia, April 2014, PloS one, 10, e0119728, 2015.

1118 Murphy, D. M.; Hudson, P. K.; Thomson, D. S.; Sheridan, P. J.; Wilson, J. C. Observations of Mercury-
1119 Containing Aerosols. Environ. Sci. Technol. 2006, 40 (10), 3163–3167.
1120
1121 Noone, D.: Pairing Measurements of the Water Vapor Isotope Ratio with Humidity to Deduce
1122 Atmospheric Moistening and Dehydration in the Tropical Midtroposphere, Journal of Climate, 25,
1123 4476–4494, https://doi.org/10.1175/JCLI-D-11-00582.1, 2012.

1124 Pisso, I., Sollum, E., Grythe, H., Kristiansen, N. I., Cassiani, M., Eckhardt, S., Arnold, D., Morton, D.,
1125 Thompson, R. L., Groot Zwaaftink, C. D., Evangeliou, N., Sodemann, H., Haimberger, L., Henne, S.,
1126 Brunner, D., Burkhart, J. F., Fouilloux, A., Brioude, J., Philipp, A., Seibert, P., and Stohl, A.: The
1127 Lagrangian particle dispersion model FLEXPART version 10.4, Geoscientific Model Development,
1128 12, 4955–4997, https://doi.org/10.5194/gmd-12-4955-2019, 2019.

1129 Polian, G., Lambert, G., Ardouin, B., and Jegou, A.: Long-range transport of continental radon in
1130 subantarctic and antarctic areas, Tellus B: Chemical and Physical Meteorology, 38, 178–189, 1986.

Risi, C., Bony, S., Vimeux, F., and Jouzel, J.: Water-stable isotopes in the LMDZ4 general circulation model: Model evaluation for present-day and past climates and applications to climatic interpretations of tropical isotopic records, Journal of Geophysical Research Atmospheres, 115, https://doi.org/10.1029/2009JD013255, 2010.

Ryan, B.F., J.J. Katzfey, D.J. Abbs, C. Jakob, U. Lohmann, B. Rockel, L.D. Rotstayn, R.E. Stewart, K.K. Szeto, G. Tselioudis, and M.K. Yau, 2000: Simulations of a cold front by cloud-resolving, limited-area, and large-scale models, and a model evaluation using in situ and satellite observations. *Mon. Weather Rev.*, **128**, 3218-3235, doi:10.1175/1520-0493(2000)

Sciare, J., Mihalopoulos, N., and Dentener, F.: Interannual variability of atmospheric dimethylsulfide in the southern Indian Ocean, Journal of Geophysical Research: Atmospheres, 105, 26369–26377, 2000.

Sciare, J., Favez, O., Sarda-Estève, R., Oikonomou, K., Cachier, H., and Kazan, V.: Long-term observations of carbonaceous aerosols in the Austral Ocean atmosphere: Evidence of a biogenic marine organic source, Journal of Geophysical Research: Atmospheres, 114, 2009.

Shah, V., Jacob, D. J., Thackray, C. P., Wang, X., Sunderland, E. M., Dibble, T. S., Saiz-Lopez, A., Cˇ ernušák, I., Kellö, V., astro, P. J., Wu, R., and Wang, C.: Improved Mechanistic Model of the Atmospheric Redox Chemistry of Mercury, Environ. Sci. Technol., 55, 14445–14456, https://doi.org/10.1021/acs.est.1c03160, 2021.

Sheu, G. R.; Lin, N. H.; Wang, J. L.; Lee, C. T.; Yang, C. F. O.; Wang, S. H. Temporal distribution and potential sources of atmospheric mercury measured at a high-elevation background station in Taiwan Atmos. Environ. 2010, 44 (20) 2393– 2400 DOI: 10.1016/j.atmosenv.2010.04.009

Sherwood, S. C., Bony, S., and Dufresne, J.-L.: Spread in model climate sensitivity traced to atmospheric convective mixing, Nature, 505, 37–42, https://doi.org/10.1038/nature12829, 2014.

Sillman, S., Marsik, F. J., Al-Wali, K. I., Keeler, G. J., and Landis, M. S.: Reactive mercury in the troposphere: Model formation and results for Florida, the northeastern United States, and the Atlantic Ocean, Journal of Geophysical Research: Atmospheres, 112, 2007.

Slemr, F., Angot, H., Dommergue, A., Magand, O., Barret, M., Weigelt, A., Ebinghaus, R., Brunke, E.-G., Pfaffhuber, K. A., Edwards, G., and others: Comparison of mercury concentrations measured at several sites in the Southern Hemisphere, Atmospheric Chemistry and Physics, 15, 3125–3133, 2015.

Slemr, F., Martin, L., Labuschagne, C., Mkololo, T., Angot, H., Magand, O., Dommergue, A., Garat, P., Ramonet, M., and Bieser, J.: Atmospheric mercury in the Southern Hemisphere–Part 1: Trend and inter-annual variations in atmospheric mercury at Cape Point, South Africa, in 2007–2017, and on Amsterdam Island in 2012–2017, Atmospheric Chemistry and Physics, 20, 7683–7692, 2020.

Sprovieri, F., Pirrone, N., Bencardino, M., D'amore, F., Carbone, F., Cinnirella, S., Mannarino, V., Landis, M., Ebinghaus, R., Weigelt, A., and others: Atmospheric mercury concentrations observed at ground-based monitoring sites globally distributed in the framework of the GMOS network, Atmospheric chemistry and physics, 16, 11915–11935, 2016.

Steen-Larsen, H. C., Johnsen, S. J., Masson-Delmotte, V., Stenni, B., Risi, C., Sodemann, H., Balslev-Clausen, D., Blunier, T., Dahl-Jensen, D., Elleh??j, M. D., Falourd, S., Grindsted, A., Gkinis, V., Jouzel, J., Popp, T., Sheldon, S., Simonsen, S. B., Sjolte, J., Steffensen, J. P., Sperlich, P., Sveinbj??rnsd??ttir, A. E., Vinther, B. M., and White, J. W. C.: Continuous monitoring of summer surface water vapor isotopic composition above the Greenland Ice Sheet, Atmospheric Chemistry and Physics, 13, 4815–4828, https://doi.org/10.5194/acp-13-4815-2013, 2013.

Mis en forme: Police :11 pt

Mis en forme: Police par défaut

Mis en forme: Corps

1177 Steffen, A., Scherz, T., Olson, M., Gay, D., and Blanchard, P.: A comparison of data quality control
1178 protocols for atmospheric mercury speciation measurements, Journal of Environmental Monitoring,
1179 14, 752–765, 2012.

1180 Stevens, B., Giorgetta, M., Esch, M., Mauritsen, T., Crueger, T., Rast, S., Salzmann, M., Schmidt, H.,
1181 Bader, J., Block, K., Brokopf, R., Fast, I., Kinne, S., Kornblueh, L., Lohmann, U., Pincus, R.,
1182 Reichler, T., and Roeckner, E.: Atmospheric component of the MPI-M Earth System Model:
1183 ECHAM6, Journal of Advances in Modeling Earth Systems, 5, 146–172,
1184 https://doi.org/10.1002/jame.20015, 2013.

1185 Swartzendruber, P., Chand, D., Jaffe, D., Smith, J., Reidmiller, D., Gratz, L., Keeler, J., Strode, S.,
1186 Jaeglé, L., and Talbot, R.: Vertical distribution of mercury, CO, ozone, and aerosol scattering
1187 coefficient in the Pacific Northwest during the spring 2006 INTEX-B campaign, Journal of
1188 Geophysical Research: Atmospheres, 113, 2008.

1189 Swartzendruber, P. C., Jaffe, D. A., Prestbo, E., Weiss-Penzias, P., Selin, N. E., Park, R., Jacob, D. J.,
1190 Strode, S., and Jaegle, L.: Observations of reactive gaseous mercury in the free troposphere at the
1191 Mount Bachelor Observatory, Journal of Geophysical Research: Atmospheres, 111, 2006.

1192 Swartzendruber, P.; Chand, D.; Jaffe, D. A.; Smith, J.; Reidmiller, D.; Gratz, L.; Keeler, J.; Strode, S.;
1193 Jaegle, L.; Talbot, R. Vertical distribution of mercury, CO, ozone, and aerosol scattering coefficient in
1194 the Pacific Northwest during the spring 2006 INTEX-B campaign. J. Geophys. Res., [Atmos.] 2008,
1195 113, D10305.
1196
1197 Talbot, R., Mao, H., Scheuer, E., Dibb, J., and Avery, M.: Total depletion of Hg in the upper
1198 troposphere–lower stratosphere, Geophysical Research Letters, 34, 2007.

1199 Talbot, R., Mao, H., Scheuer, E., Dibb, J., Avery, M., Browell, E., Sachse, G., Vay, S., Blake, D.,
1200 Huey, G., and others: Factors influencing the large-scale distribution of Hg° in the Mexico City area
1201 and over the North Pacific, Atmospheric Chemistry and Physics, 8, 2103–2114, 2008.

1202 Taylor, K. E., Williamson, D., and Zwiers, F.: The sea surface temperature and sea ice concentration
1203 boundary conditions for AMIP II simulations", PCMDI Report 60, Program for Climate Model
1204 Diagnosis and Intercomparison,Lawrence Livermore National Laboratory, 2000.

1205 Thurnherr, I., Kozachek, A., Graf, P., Weng, Y., Bolshiyanov, D., Landwehr, S., Pfahl, S., Schmale,
1206 J., Sodemann, H., Steen-Larsen, H. C., and others: Meridional and vertical variations of the water
1207 vapour isotopic composition in the marine boundary layer over the Atlantic and Southern Ocean,
1208 Atmospheric Chemistry and Physics, 20, 5811–5835, 2020.

1209 Tremoy, G., Vimeux, F., Cattani, O., Mayaki, S., Souley, I., and Favreau, G.: Measurements of water
1210 vapor isotope ratios with wavelength-scanned cavity ring-down spectroscopy technology: New
1211 insights and important caveats for deuterium excess measurements in tropical areas in comparison
1212 with isotope-ratio mass spectrometry, Rapid Communications in Mass Spectrometry, 25, 3469–3480,
1213 https://doi.org/10.1002/rcm.5252, 2011.

1214 Tremoy, G., Vimeux, F., Mayaki, S., Souley, I., Cattani, O., Risi, C., Favreau, G., and Oi, M.: A 1-
1215 year long δ18O record of water vapor in Niamey (Niger) reveals insightful atmospheric processes at
1216 different timescales, Geophysical Research Letters, 39, 2012.

1217 Tremoy, G., Vimeux, F., Soumana, S., Souley, I., Risi, C., Favreau, G., and Oï, M.: Clustering
1218 mesoscale convective systems with laser-based water vapor δ18O monitoring in Niamey (Niger),
1219 Journal of Geophysical Research: Atmospheres, 119, 5079–5103,
1220 https://doi.org/10.1002/2013JD020968, 2014.

Wang, H., Fyke, J. G., Lenaerts, J. T. M., Nusbaumer, J. M., Singh, H., Noone, D., Rasch, P. J., and Zhang, R.: Influence of sea-ice anomalies on Antarctic precipitation using source attribution in the Community Earth System Model, The Cryosphere, 14, 429–444, https://doi.org/10.5194/tc-14-429-2020, 2020.

Weiss-Penzias, P.; Gustin, M. S.; Lyman, S. N. Observations of speciated atmospheric mercury at three sites in Nevada: Evidence for a free tropospheric source of reactive gaseous mercury. J. Geophys. Res. [Atmos.] 2009, 114, D14302.

Weng, Y., Touzeau, A., and Sodemann, H.: Correcting the impact of the isotope composition on the mixing ratio dependency of water vapour isotope measurements with cavity ring-down spectrometers, Atmospheric Measurement Techniques, 13, 3167–3190, https://doi.org/10.5194/amt-13-3167-2020, 2020.

Worden, J., Noone, D., and Bowman, K.: Importance of rain evaporation and continental convection in the tropical water cycle., Nature, 445, 528–532, https://doi.org/10.1038/nature05508, 2007.

Mis en forme: Police :(Par défaut) Times New Roman, 11 pt

Mis en forme: Police par défaut, Couleur de police : Noir

Mis en forme: Corps

Mis en forme: Normal

Mis en forme: Contour du texte

1238